Thermochemically-Closed Sonic-Flow Inversion for Enthalpy and Temperature in Multispecies Arc-Jet Flows

Jocelino Rodrigues*
NASA Postdoctoral Program via ORAU at NASA Ames Research Center, Moffett Field, CA 94035, USA

A thermochemically-closed sonic-flow inversion framework (TSIF) is developed to infer bulk enthalpy and total temperature upstream of a choked nozzle in multi-species arc-jet flows. The formulation recasts a pressure-rise total enthalpy quantification technique as an inverse problem in characteristic-velocity c^* space using measured mass flow rate, upstream total pressure, gas composition, and nozzle throat geometry as inputs. Unlike calorimetric energy-balance approaches or optical diagnostics, the method relies on upstream facility measurements and explicit thermochemical closure, without requiring downstream heat-flux, spectroscopic, calorimetric, or CFD-derived inputs. Thermochemical states are obtained using NASA's open-source Chemical Equilibrium with Applications (CEA) code, enabling construction of a relationship between characteristic velocity, total enthalpy, and total temperature under equilibrium or frozen assumptions. A discharge coefficient is self-calibrated using cold-flow (arc-off) data and applied to hot-flow (arc-on) measurements, allowing repeatable facility- and nozzle-level non-idealities to be represented through an explicit effective correction without empirical enthalpy correlations. The framework is applied to air, N_2, and CO_2/N_2 arc-jet flows in the 30 kW mARC II facility, demonstrating expected trends with arc power, specific energy input, mass flow rate, and heater configuration, as well as composition-dependent variation in inferred bulk enthalpy. The inferred enthalpies also enable characterization of arc-jet efficiency, while equilibrium–frozen comparisons quantify sensitivity to chemical-relaxation assumptions. In the equilibrium-air limit, the method recovers the classical high-enthalpy asymptotic relation of Winovich with a mean residual of 4.4%, demonstrating compatibility with established sonic-flow scaling while extending applicability to specified multi-species mixtures and selectable equilibrium/frozen chemical models. The framework provides a mixture-flexible methodology for determining bulk thermochemical states in modern arc-jet environments using existing facility instrumentation and without requiring additional diagnostic hardware.

Nomenclature

Symbols

h	=	enthalpy	T	=	temperature
$\dot{m}_{\mathrm{T}}$	=	total mass flow rate	A	=	area
p	=	pressure	M	=	Mach number
ρ	=	density	c_p	=	specific heat capacity
C_d	=	discharge coefficient	γ	=	specific heat ratio
c^*	=	characteristic velocity	Y	=	mass fraction
$\bar{u}$	=	bulk velocity	MW	=	molecular weight
I_{arc}	=	arc current	P_{arc}	=	arc power
σ	=	standard deviation	η	=	arc-jet efficiency

Subscripts/Superscripts

$(\cdot)_0$	=	total (stagnation) quantity	$(\cdot)_{\mathrm{bulk}}$	=	bulk quantity
$(\cdot)_{\mathrm{TP}}$	=	relating to CEA's TP problem	$(\cdot)_{\mathrm{ref}}$	=	reference quantity
$(\cdot)_{\mathrm{ROCKET}}$	=	relating to CEA's ROCKET problem	$(\cdot)^{\mathrm{abs}}$	=	absolute quantity
$(\cdot)_{\mathrm{cold}}$	=	relating to cold-flow (arc-off) conditions	$(\cdot)^{\mathrm{eq}}$	=	relating to equilibrium chemical model
$(\cdot)_{\mathrm{hot}}$	=	relating to hot-flow (arc-on) conditions	$(\cdot)^{\mathrm{fr}}$	=	relating to frozen chemical model
$(\cdot)_{\mathrm{exp}}$	=	relating to experimental measurement	$(\cdot)_{\mathrm{t}}$	=	relating to nozzle throat

*NPP Research Fellow, Thermophysics Facilities Branch, Entry Systems & Technology Division. AIAA Young Professional. (✉ jocelino.rodrigues@nasa.gov).

I. Introduction

High-enthalpy arc-jet facilities are widely used to reproduce the coupled thermal, chemical, radiative, and fluid-dynamic environments encountered during atmospheric entry [1, 2]. Accurate quantification of the bulk enthalpy of the test flow remains a central requirement for both experimental interpretation and numerical model validation [3, 4]. In particular, bulk enthalpy provides a primary in-flow boundary condition for computational fluid dynamics (CFD) simulations of test articles, directly influencing predicted heat fluxes, shock-layer chemistry, and surface response [5]. Errors in estimated bulk enthalpy propagate non-linearly into reconstructed entry conditions, undermining comparisons between ground tests, numerical models, and flight data [6, 7]. Bulk enthalpy is not directly measured as a primitive thermodynamic state variable in arc-jet facilities; instead, it is reconstructed from measurable quantities through energy balances, sonic-flow theory, correlations, or spectroscopic inference, each requiring specific modeling assumptions and thermodynamic closure. Consequently, the inferred value depends on the physical constraints imposed by the chosen methodology.

From a physical standpoint, bulk enthalpy in an arc-jet flow is commonly used to characterize the total energy content of the upstream arc-heater column feeding the nozzle, including both sensible thermal energy and chemical energy associated with dissociation and excitation [8]. Here, *bulk* refers specifically to the upstream nozzle-feed state rather than nozzle-exit, free-jet, or test-section conditions. Under choked-flow conditions, this bulk enthalpy governs the thermodynamic state reached at the nozzle throat. Through this throat state, it controls the characteristic velocity of the choked nozzle flow and the kinetic energy available at the nozzle exit. This relationship links arc-jet enthalpy operating conditions to realistic flight profiles via an effective entry velocity v_∞ through the familiar scaling $h_0 \sim v_\infty^2/2$ [9]. Consequently, reliable enthalpy inference is essential for establishing ground-to-flight equivalence between arc-jet test conditions and flight-relevant entry trajectories [10].

Several techniques have historically been employed to infer bulk enthalpy in arc-jet flows [11–19]. Two early formulations were proposed by Winovich [11]: an equilibrium-air sonic-flow relation for enthalpy and a companion pressure-rise formulation derived from the same choking relations, with additional discussion of frozen-flow and real-flow correction effects. While the equilibrium sonic-flow correlation has become standard in arc-jet analysis, the companion pressure-rise formulation has seen limited subsequent adoption in the literature. The pressure-rise formulation is based on the same sonic-flow relations and uses the increase in total pressure between cold-flow (arc-off) and hot-flow (arc-on) conditions when the choked mass flow rate through the throat is matched for both test conditions. Later updates to the sonic-flow method—including those developed by Shepard et al. [12], Thompson et al. [15], and Palmer et al. [5]—continued to provide air-specific sonic-flow relations and correlations over restricted total pressure and total enthalpy ranges. These relations remain widely used because they provide a practical and well-established starting point for arc-jet analysis. Their sonic-flow basis shares the simplifying assumptions common to many choked-flow methods, including one-dimensional, adiabatic, and isentropic nozzle flow, with equilibrium air typically serving as the baseline formulation. Although correction procedures for frozen-flow and real-flow effects were considered in the original Winovich work, the commonly used correlations remain primarily air-specific and are applied over finite pressure and enthalpy ranges. Direct application to non-air mixtures, alternative chemistry models, or extrapolated operating conditions requires caution.

In parallel, the energy-balance technique detailed in the ASTM E341-08 standard [18] estimates arc-gas enthalpy from an integrated facility energy balance. In this approach, the energy retained by the flow is inferred from the electrical power delivered to the heater after accounting for heat removed by coolant circuits in the cathode, arc column, anode, mixing plenum, and nozzle. However, the uncertainty of this calorimetric approach can become significant when coolant temperature rises ΔT are small, particularly when the inferred gas enthalpy is obtained from the difference between large input-power and coolant heat-removal terms. A practical limitation of calorimetric approaches is that they rely on facility-specific cooling architectures and well-resolved coolant energy balances. This dependence is particularly restrictive for facilities, such as inductively coupled plasma (ICP) torches, where the flowpath and energy addition mechanisms, including non-trivial RF power coupling and distributed losses, do not generally permit ASTM-style coolant calorimetry in a form directly analogous to arc-heater designs [20].

More recently, non-intrusive optical and laser diagnostics, including absorption and fluorescence spectroscopy, have demonstrated the capability to estimate reservoir temperature and enthalpy within the plenum of different high-enthalpy facilities [19, 21–26]. These diagnostics provide high-frequency, non-intrusive measurements of local flow properties, yielding detailed insight into the challenging environments of high-enthalpy facilities. However, such techniques generally rely on equilibrium or near-equilibrium spectral modeling and on species-specific features. As a result, implementation requires wavelength selection, laser hardware, and calibration procedures tailored to the gas mixture of interest, which can limit diagnostic flexibility.

While bulk enthalpy remains the primary quantity of interest in arc-jet testing, the associated reservoir total temperature is also difficult to quantify and provides an important descriptor of the thermodynamic state. Thermochemical and non-equilibrium flow simulations exhibit strong temperature sensitivity through reaction rates, transport properties, internal energy mode excitation, and radiative emission [8, 27–30]. Likewise, interpretation of plasma diagnostics, including optical emission spectroscopy, radiation modeling, and collisional–radiative analyses, requires temperature information to relate measured signals to species populations and excitation states [22, 24, 31–35]. Although such diagnostics may involve local or mode-specific temperatures, a consistent reservoir-scale total temperature provides a useful reference state. Reliable estimates of total temperature are therefore also valuable.

Although the aforementioned approaches have proven effective within their intended domains, they exhibit limitations when extended to modern arc-jet applications involving non-air mixtures, multi-species flows, or alternative chemical assumptions. Such constraints can restrict generality, complicate direct application to mixed flows, and may not explicitly enforce consistency between measured total mass flow, upstream total pressure, and thermochemical state at the nozzle throat. This motivates the proposed thermochemically-closed sonic-flow inversion framework (TSIF), which treats choking as the primary observation model and enforces a selectable thermochemical closure to infer bulk enthalpy and total temperature in the reservoir upstream of a choked nozzle.

The present work makes three contributions. First, it reformulates the pressure-rise choking constraint as a characteristic-velocity inversion with explicit thermochemical closure. Second, it introduces a cold-flow self-calibration that accounts for repeatable departures from ideal quasi-one-dimensional choking without gas-specific empirical enthalpy correlations. Third, it applies the framework to air, N_2, and CO_2/N_2 mixtures under equilibrium and frozen assumptions, demonstrating recovery of classical equilibrium-air sonic-flow scaling as a limiting case.

II. Inversion framework

The TSIF approach extends the classical air-focused sonic-flow framework of Winovich [11] through a thermochemically-closed inversion formulated in characteristic-velocity space. Following the framework employed by Winovich [11], the total mass flow rate through a choked, one-dimensional, homogeneous, adiabatic, isentropic nozzle is governed by:

$$\dot{m}_\mathrm{T} = \frac{p_0 A_t}{c^*} , \tag{1}$$

where $\dot{m}_\mathrm{T}$ is the total mass flow rate, p_0 is the upstream total pressure, A_t is the nozzle throat area, and c^* is the characteristic velocity corresponding to the upstream thermochemical state [36].

Instead of relying on published gas-specific sonic-flow relations or enthalpy correlations, the present method uses NASA's Chemical Equilibrium with Applications (CEA) code to construct a thermochemical relationship between characteristic velocity (c^*), total enthalpy (h_0), and total temperature (T_0) at the measured upstream total pressure (p_0) [37–43]. The inversion is performed directly in c^*-space, consistent with the governing choking constraint. CEA is used in the present work because it is publicly available, widely used in high-temperature gas-dynamics applications, and provides a reproducible thermochemical closure for both equilibrium and frozen nozzle-flow calculations. The inversion framework itself, however, is not specific to CEA. Any thermochemical solver capable of providing a self-consistent c^*–h_0–T_0 manifold for the specified upstream total pressure, gas composition, and chemical-relaxation model could be used. Quantitative differences between solvers may arise from differences in thermodynamic databases, species sets, reference enthalpies, condensed-phase treatment, and the implementation of the selected chemistry model.

Repeatable departures from the ideal quasi-one-dimensional choking model are incorporated into Eq. (1) through an effective discharge coefficient (C_d), which is calibrated from steady-state cold-flow (arc-off) measurements and subsequently applied during hot-flow (arc-on) operation. In this formulation, C_d represents a facility- and nozzle-level correction for the measured choked-flow response rather than a decomposition of individual flow or heat-transfer mechanisms. The resulting C_d-corrected characteristic velocity is then used to infer the corresponding hot-flow thermodynamic state. The primary reported quantity is the net total enthalpy rise between hot-flow and cold-flow conditions, denoted throughout this work as the bulk enthalpy diagnostic quantity, $h_\mathrm{bulk} \equiv \Delta h_0$. This diagnostic quantity is inferred from the measured choking response of the facility, and its relationship with the classical mass-flux-weighted definition of bulk enthalpy is discussed in §II.E.

The inversion framework requires measurements of total mass flow rate, measured upstream total pressure during cold-flow and hot-flow operation, nozzle throat geometry, cold-flow inlet temperature, and injected gas composition. The governing observation model and thermochemical closure are formalized in the following subsection.

A. Governing relation and thermochemical closure

The upstream arc column is modeled as a quasi-one-dimensional reservoir feeding a choked nozzle throat of area A_t [36]. Equation (1) describes the ideal isentropic mass flow rate for sonic conditions at the throat ($M_t = 1$). Retaining the effective discharge coefficient C_d introduced in the opening discussion of this section, the corresponding constant-γ choking relation may be written as:

$$\frac{\dot{m}_\mathrm{T}}{A_t} = C_d\, p_0 \sqrt{\frac{\gamma}{R\,T_0}} \left(\frac{2}{\gamma+1}\right)^{\frac{\gamma+1}{2(\gamma-1)}} , \tag{2}$$

where γ is the effective specific heat ratio and R is the specific gas constant corresponding to the local thermochemical state.

Equation (2) defines the measurement-based observation model. Re-arranging gives an effective characteristic velocity:

$$c^*_\mathrm{eff} = C_d\, c^*_\mathrm{exp} = C_d \left(\frac{p_0 A_t}{\dot{m}_\mathrm{T}}\right) = \sqrt{\frac{R\,T_0}{\gamma}} \left(\frac{\gamma+1}{2}\right)^{\frac{\gamma+1}{2(\gamma-1)}} , \tag{3}$$

where $c^*_\mathrm{exp} = p_0 A_t/\dot{m}_\mathrm{T}$ is the characteristic velocity obtained directly from the measured choking response.

Equation (3) is shown in its compact constant-γ form for reference. In practice, the thermochemical inversion matches the corrected characteristic velocity c^*_eff to the characteristic velocity predicted by the CEA solution, which accounts for temperature-dependent thermodynamic properties and chemistry effects. The corresponding thermodynamic state is obtained by identifying the (T_0, h_0) pair on the CEA-generated thermochemical manifold at fixed total pressure p_0. In this work, $h_0(p_0, T_0)$ denotes the CEA-reported thermochemical enthalpy associated with the upstream station 1 state. Since station 1 is modeled as a stagnation reservoir with negligible bulk kinetic energy, this quantity is interpreted as the upstream total enthalpy h_0 and is referenced to a common baseline temperature T_ref:

$$h_0(p_0, T_0) \equiv h_0^\mathrm{abs}(p_0, T_0) - h_0^\mathrm{abs}(p_0, T_\mathrm{ref}) , \qquad T_\mathrm{ref} = 298.15\ \mathrm{K} . \tag{4}$$

For interpretation, the referenced stagnation enthalpy of a reacting multi-species flow may be viewed schematically as containing sensible, chemical-composition, and kinetic contributions:

$$h_0 = \underbrace{h_\mathrm{sensible}}_{\sum_{i=1}^{N_i} Y_i \int_{T_\mathrm{ref}}^{T} c_{p,i}(T')\, dT'} + \underbrace{h_\mathrm{chemical}}_{\sum_{i=1}^{N_i} Y_i \Delta h^\circ_{f,i}} + \underbrace{h_\mathrm{kinetic}}_{\frac{\bar{u}^2}{2}} , \tag{5}$$

where Y_i is the species mass fraction, $c_{p,i}$ is the species-specific heat capacity, $\Delta h^\circ_{f,i}$ is the standard enthalpy of formation relative to the elemental reference state, and $\bar{u}$ is the bulk flow velocity [44]. Equation (5) is intended as a schematic decomposition highlighting that high-enthalpy flows may contain substantial energy contributions associated with sensible heating, chemical composition, dissociation/recombination, and bulk kinetic energy. In the present quasi-one-dimensional reservoir formulation, the upstream kinetic contribution is assumed negligible relative to the total enthalpy. The inferred upstream state is governed primarily by the sensible and chemical components represented within the CEA thermochemical solution. All enthalpies are expressed in MJ/kg.

Two limiting thermochemical relaxation models are enforced through CEA: equilibrium and frozen. In the equilibrium formulation, total pressure p_0 and total temperature T_0 are first used as inputs, and then CEA evaluates mixture composition and thermodynamic properties for an ideal-gas mixture using Gibbs free-energy minimization subject to elemental conservation. The species mass fractions adjust continuously with pressure and temperature according to chemical equilibrium during quasi-one-dimensional acceleration from the reservoir stagnation state to the choked throat condition. As a result, the resulting characteristic velocity $c^*(p_0, T_0)$ reflects full thermochemical relaxation consistent with equilibrium composition at the sonic state. This is the standard thermochemical equilibrium model used in high-temperature gas dynamics.

In the frozen formulation, the reservoir composition is first established at the specified total pressure p_0 and total temperature T_0 state, after which the species mass fractions are held fixed during quasi-one-dimensional acceleration to the throat. Chemical recombination is suppressed during acceleration, and the resulting c^* reflects a non-equilibrium limiting representation of the choked condition with composition frozen at the stagnation state. This corresponds to the limiting case of infinitely slow chemical relaxation.

In both formulations, condensed phases are omitted and the mixture is constrained to remain gas-phase only. The distinction between equilibrium and frozen solutions arises solely from the thermochemical relaxation model selected within CEA. In practical arc-jet operation, the validity of these limits depends on the relative magnitudes of chemical relaxation timescales and flow residence times, as well as the pressure level and degree of dissociation within the arc column. Real arc-heater flows may exhibit partial non-equilibrium behavior lying between the equilibrium and frozen limits. The present inversion framework does not explicitly resolve finite-rate or collisional–radiative chemistry; rather, equilibrium and frozen compositions are treated as limiting thermochemical models within which the macroscopic choked-flow inversion is performed.

Within this framework, CEA provides thermochemical closure through the selected chemistry model, while Eq. (2) provides the compressible-flow observation model linking facility measurements to the upstream state. The two components are coupled only through characteristic velocity, preserving structural separation between the measurement model and the thermochemical state model. Previous sonic-flow formulations often employ the reciprocal of c^* (the sonic-flow parameter), and do not explicitly retain a separately calibrated discharge correction in the form used here [5, 11, 45, 46].

The cold-flow calibration that determines the discharge correction is described in §II.B; its application to the arc-on inversion is then described in §II.C.

B. Cold-flow reference state and discharge coefficient calibration

The first step of the inversion framework uses steady-state cold-flow (arc-off) measurements to establish the reference enthalpy $h_{0,\text{cold}}$ and determine the discharge correction C_d for the run, as shown in Fig. 1. In this formulation, C_d maps the measured cold-flow choking response onto the ideal quasi-one-dimensional thermochemical prediction for the same cold-flow stagnation state. It is treated as an effective facility- and nozzle-level correction for repeatable departures from the ideal choking model, rather than as a decomposition of individual loss mechanisms.

Cold-flow thermodynamic properties are obtained from an equilibrium *TP* problem evaluation for numerical robustness. The *TP* formulation is used for the cold-flow reference state because the CEA *ROCKET* calculation can be numerically unstable near room-temperature conditions, whereas the *TP* problem provides a stable evaluation of the same inlet thermochemical state:

$$c^*_{\text{TP}} \equiv c^*_{\text{TP}}(p_{0,\text{cold}}, T_{0,\text{cold}}) \,, \tag{6}$$

$$h_{0,\text{cold}} \equiv h_0(p_{0,\text{cold}}, T_{0,\text{cold}}) = h_0^{\text{abs}}(p_{0,\text{cold}}, T_{0,\text{cold}}) - h_0^{\text{abs}}(p_{0,\text{cold}}, T_{\text{ref}}) \,, \tag{7}$$

where $T_{0,\text{cold}} \approx T_{\text{in}}$ under cold-flow conditions. At these temperatures, the equilibrium composition remains effectively equal to the injected gas composition, so dissociation and ionization are negligible for the cold-flow reference calculation.

The cold-flow characteristic velocity obtained directly from the steady-state experimental measurements is:

$$c^*_{\text{exp,cold}}(p_{0,\text{cold}}) = \frac{p_{0,\text{cold}} A_t}{\dot{m}_{\text{T}}} \,. \tag{8}$$

The experimentally inferred cold-flow characteristic velocity from Eq. (8) is then compared with the ideal CEA prediction from Eq. (6):

$$C_d = \frac{c^*_{\text{TP}}(p_{0,\text{cold}}, T_{0,\text{cold}})}{c^*_{\text{exp,cold}}(p_{0,\text{cold}})} \,. \tag{9}$$

For the present measurements, the calibrated values satisfy $C_d < 1$, consistent with an effective correction relative to the ideal quasi-one-dimensional choking prediction. The inferred C_d value is subsequently held fixed during hot-flow inversion (see §II.C). Differences between cold-flow and hot-flow operation are inferred through changes in the upstream thermochemical state, not through adjustment of the discharge correction.

C. Hot-flow inversion

The second step of the inversion framework involves steady-state measurements during hot-flow (arc-on), as shown in Fig. 1. For the hot-flow condition, CEA *ROCKET* is first used to construct a fixed-pressure thermochemical manifold relating c^*_{ROCKET}, h_0, and T_0 at the measured upstream total pressure $p_{0,\text{hot}}$:

$$c^*_{\text{ROCKET}} \equiv c^*_{\text{ROCKET}}(p_{0,\text{hot}}, T_{0,k}) \,, \tag{10}$$

$$h_0(p_{0,\text{hot}}, T_{0,k}) = h_0^{\text{abs}}(p_{0,\text{hot}}, T_{0,k}) - h_0^{\text{abs}}(p_{0,\text{hot}}, T_{\text{ref}}) \,, \tag{11}$$

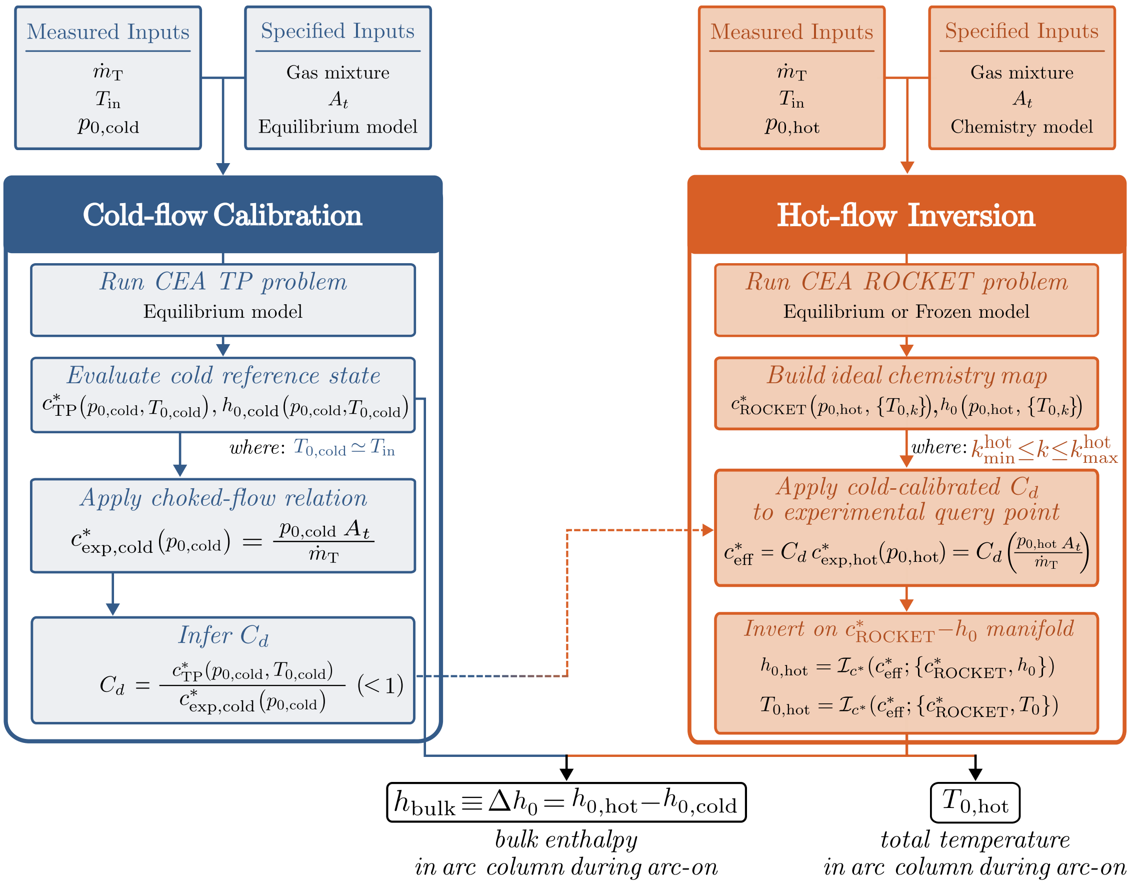

Fig. 1 Process diagram illustrating TSIF for inferring bulk enthalpy and total temperature.

where the upstream total temperature is varied over a grid $1000 \le T_{0,k} \le 12{,}000$ K, mapped at every $\Delta T_0 = 25$ K, yielding paired values $\left(c^*_{ROCKET}(p_{0,hot}, T_{0,k}),\ h_0(p_{0,hot}, T_{0,k})\right)$. This pre-inference mapping defines a single-valued thermochemical manifold:

$$c^*_{ROCKET} \longleftrightarrow h_0\ , \tag{12}$$

for fixed $p_{0,hot}$, gas composition, and chemistry model (equilibrium or frozen).

Independently, the characteristic velocity obtained directly from the steady-state hot-flow measurements is:

$$c^*_{exp,hot}(p_{0,hot}) = \frac{p_{0,hot} A_t}{\dot{m}_T}\ . \tag{13}$$

The cold-flow calibration described in §II.B provides the discharge correction used to compute the effective characteristic velocity for the hot-flow inversion:

$$c^*_{eff} = C_d\, c^*_{exp,hot}(p_{0,hot}) = C_d \left(\frac{p_{0,hot} A_t}{\dot{m}_T}\right)\ . \tag{14}$$

The discharge correction modifies only the query location in c^*-space; it does not alter the CEA-generated thermochemical manifold.

Substituting the cold-flow calibration from Eq. (9) into Eq. (14) gives an equivalent pressure-rise form:

$$c^*_{eff} = c^*_{TP}(p_{0,cold}, T_{0,cold}) \left(\frac{\dot{m}_{T,cold}}{p_{0,cold} A_t}\right) \left(\frac{p_{0,hot} A_t}{\dot{m}_{T,hot}}\right)\ . \tag{15}$$

For matched cold-flow and hot-flow mass flow rates, $\dot{m}_{T,hot} = \dot{m}_{T,cold}$, the throat area and mass flow ratio cancel:

$$c^*_{eff} = c^*_{TP}(p_{0,cold}, T_{0,cold}) \left(\frac{p_{0,hot}}{p_{0,cold}}\right)\ . \tag{16}$$

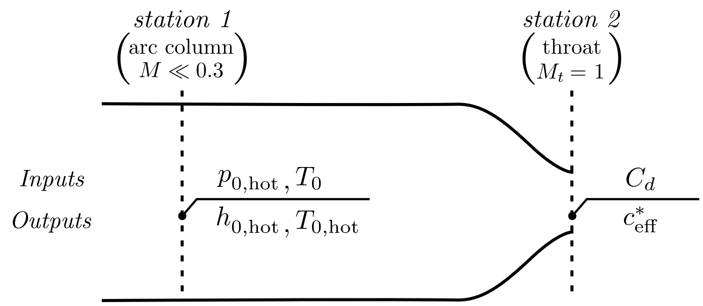

Fig. 2 Quasi-1D station definition used in the CEA *ROCKET* formulation: station 1 represents the stagnation reservoir and station 2 represents the choked nozzle throat.

Equation (16) is a central result of the formulation because it shows that the self-calibrated method is fundamentally a thermochemically-closed pressure-rise technique expressed in c^*-space. It also shows that A_t cancels exactly and that common-mode mass flow calibration uncertainty cancels when cold-flow and hot-flow total mass flow rates are matched.

The inversion then consists of matching the experimentally derived query value c^*_{eff} to the precomputed c^*_{ROCKET}–h_0 manifold and interpolating to recover the corresponding thermochemical state:

$$h_{0,\mathrm{hot}} \approx \mathcal{I}\left(c^*_{\mathrm{eff}}; \{c^*_{\mathrm{ROCKET}}(p_{0,\mathrm{hot}}, T_{0,k}),\ h_0(p_{0,\mathrm{hot}}, T_{0,k})\}\right) . \tag{17}$$

Here $\mathcal{I}$ denotes bounded linear interpolation in c^*-space. The interpolated manifold point yields both the inferred arc-on total enthalpy $h_{0,\mathrm{hot}}$ and the corresponding total temperature $T_{0,\mathrm{hot}}$, because each point on the pre-inference mapping is associated with a prescribed $T_{0,k}$. For the thermochemical states considered here, the c^*_{ROCKET}–h_0 relationship remains monotonic over the admissible temperature range for both thermochemical models (equilibrium and frozen), ensuring a unique inversion.

Figure 3 illustrates an example thermochemical manifold for an equilibrium 95% CO_2/5% N_2 mixture at fixed total pressure $p_{0,\mathrm{hot}}$. The experimentally derived value c^*_{eff} defines the query location in c^*-space, while the manifold itself is determined entirely by the selected CEA chemistry model at the measured upstream total pressure p_0. The inferred thermochemical state corresponds to the unique manifold point whose characteristic velocity matches the measured choking response. For the illustrated case ($\dot{m}_\mathrm{T}$ = 0.30 g/s, $p_{0,\mathrm{hot}}$ = 32.5 kPa, $p_{0,\mathrm{cold}}$ = 5.3 kPa, T_in = 295 K, T_ref = 298.15 K), the inversion yields $h_{0,\mathrm{hot}}$ = 18.9 MJ/kg and $T_{0,\mathrm{hot}}$ = 5465 K (assuming equilibrium chemistry).

The primary derived diagnostic quantity reported in this work is the net total enthalpy rise between hot-flow and cold-flow conditions:

$$h_\mathrm{bulk} \equiv \Delta h_0 = h_{0,\mathrm{hot}} - h_{0,\mathrm{cold}} , \tag{18}$$

where h_bulk is used throughout this paper to denote the inferred bulk enthalpy diagnostic quantity. For the case shown in Fig. 3, $h_{0,\mathrm{cold}} = -0.0026$ MJ/kg because the cold-flow inlet temperature $T_\mathrm{in} = 295$ K is close to the reference temperature $T_\mathrm{ref} = 298.15$ K. This gives $h_\mathrm{bulk} \equiv \Delta h_0 \simeq h_{0,\mathrm{hot}}$ for this case. The inlet temperature T_in enters the reported bulk enthalpy only through the cold-flow reference enthalpy $h_{0,\mathrm{cold}}$ (see §II.B); the hot-flow state $(h_{0,\mathrm{hot}}, T_{0,\mathrm{hot}})$ is obtained independently from inversion of c^*_{eff} at the measured $p_{0,\mathrm{hot}}$. For consistency with the thermodynamic definition, all reported values are nevertheless computed as $h_{0,\mathrm{hot}} - h_{0,\mathrm{cold}}$.

The present method constitutes an independent thermochemical framework. Agreement or discrepancy with bulk enthalpy values inferred using empirical correlations, calorimetric standards, spectroscopic diagnostics, or CFD-based approaches should be interpreted in light of combined experimental uncertainty, diagnostic sensitivity, and modeling assumptions. In practice, calorimetric approaches depend on multiple independently calibrated measurements and may exhibit elevated relative uncertainty when coolant temperature rises are small. Spectroscopic methods introduce line-of-sight integration and model-form sensitivities associated with spatial inhomogeneities and non-equilibrium plasmas. By comparison, the present inversion relies primarily on measurements of upstream total pressure and total mass flow rate, concentrating uncertainty into a smaller set of directly measurable quantities, notably $p_{0,\mathrm{hot}}$, $p_{0,\mathrm{cold}}$, and $\dot{m}_\mathrm{T}$, that can be propagated explicitly in an uncertainty analysis.

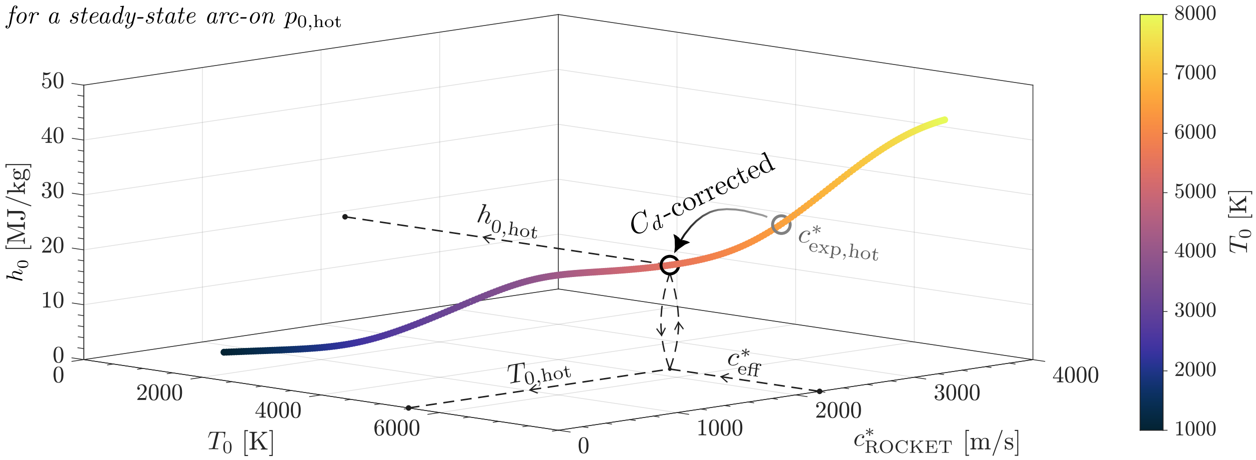

Fig. 3 Characteristic-velocity inversion manifold at fixed $p_{0,\text{hot}}$: CEA-predicted c^*_{ROCKET} plotted against total enthalpy h_0 and total temperature T_0. The inferred thermochemical hot-flow state $(h_{0,\text{hot}}, T_{0,\text{hot}})$ corresponds to the manifold point matching the C_d-corrected experimental query value $c^*_{\text{eff}} = C_d\, c^*_{\text{exp,hot}}$.

D. Uncertainty analysis

Since the inversion is performed in characteristic-velocity space, the sensitivity of the inferred thermochemical state can be interpreted directly through perturbations in the effective characteristic velocity. Using Eq. (14) for the effective hot-flow characteristic velocity, the relative standard uncertainty may be approximated as:

$$\left(\frac{\sigma_{c^*_{\text{eff}}}}{c^*_{\text{eff}}}\right)^2 \approx \left(\frac{\sigma_{C_d}}{C_d}\right)^2 + \left(\frac{\sigma_{p_{0,\text{hot}}}}{p_{0,\text{hot}}}\right)^2 + \left(\frac{\sigma_{A_t}}{A_t}\right)^2 + \left(\frac{\sigma_{\dot{m}_\text{T}}}{\dot{m}_\text{T}}\right)^2 . \tag{19}$$

As shown by Eq. (16), when the cold-flow and hot-flow mass flow rates are matched for the same nozzle geometry, the throat area cancels exactly and common-mode mass flow calibration uncertainty cancels. In this matched-flow pressure-rise form, the leading uncertainty in the corrected characteristic-velocity query is associated with the measured pressure ratio:

$$\left(\frac{\sigma_{c^*_{\text{eff}}}}{c^*_{\text{eff}}}\right)^2 \approx \left(\frac{\sigma_{p_{0,\text{hot}}}}{p_{0,\text{hot}}}\right)^2 + \left(\frac{\sigma_{p_{0,\text{cold}}}}{p_{0,\text{cold}}}\right)^2 , \tag{20}$$

where uncertainty in the cold-flow thermochemical reference value $c^*_{\text{TP}}(p_{0,\text{cold}}, T_{0,\text{cold}})$ is neglected relative to the pressure measurements. Equation (19) is retained as a conservative independent-input sensitivity form; the inclusion of A_t, $\dot{m}_\text{T}$, and C_d likely overestimates the uncertainty in c^*_{eff} for matched-flow operation.

Since $h_{0,\text{hot}}$ is obtained by interpolation on a monotonic c^*_{ROCKET}–h_0 manifold at fixed $p_{0,\text{hot}}$, the fixed-pressure contribution to the enthalpy uncertainty may be approximated locally as:

$$\sigma_{h_{0,\text{hot}}} \approx \left| \left(\frac{\partial h_0}{\partial c^*_{\text{ROCKET}}}\right)_{p_{0,\text{hot}}} \right| \sigma_{c^*_{\text{eff}}} . \tag{21}$$

The compact sensitivity form in Eq. (21) represents the local response along a fixed upstream total pressure thermochemical manifold. The same analysis applies to the cold-flow enthalpy estimate. A full uncertainty propagation would also account for perturbations of the manifold itself due to uncertainty in the upstream total pressure p_0 for the corresponding hot-flow or cold-flow state.

The uncertainty in the reported bulk enthalpy diagnostic quantity is then obtained by propagating Eq. (18). Neglecting covariance between the hot-flow and cold-flow enthalpy:

$$\sigma_{h_{\text{bulk}}} \approx \sqrt{\sigma^2_{h_{0,\text{hot}}} + \sigma^2_{h_{0,\text{cold}}}} . \tag{22}$$

E. Scope, strengths, and limitations

It is important to clarify the thermodynamic interpretation of the inferred quantities, together with the principal assumptions and limitations of the quasi-one-dimensional formulation. In arc-jet practice, bulk enthalpy typically denotes a mass-flux-weighted cross-sectional average:

$$h_{\text{bulk}}^{\text{MF}} = \frac{\int_A \rho u h \, dA}{\int_A \rho u \, dA} , \tag{23}$$

where ρ is density, u is velocity, and A is cross-sectional area, such that regions carrying higher mass flux dominate the bulk enthalpy value (e.g., the arc core relative to the near-wall boundary layer) [13].

Similar to Eq. (23), Eq. (18) does not resolve spatial temperature, velocity, or species inhomogeneities [47, 48]. Accordingly, when such inhomogeneities are significant, the inferred thermodynamic state from which h_{bulk} is derived using Eq. (18) remains meaningful, but should be interpreted as the effective condition governing nozzle choking rather than as a strict mass-flux-weighted cross-sectional average of the upstream reservoir.

Reservoir inhomogeneity can arise through three primary fields in high-enthalpy flows: temperature, velocity, and species composition. First, temperature gradients affect the inferred state through the same mass-flux weighting implicit in Eq. (23). Cold boundary layers, core–annulus structure, or other radial temperature gradients can cause cooler, denser regions to contribute disproportionately to the choked mass flow. The resulting choking response may then correspond to an effective thermodynamic state below the peak core condition, even though it remains representative of the flow state controlling the measured mass flux. Second, velocity inhomogeneity introduces ambiguity through the kinetic-energy contribution in Eq. (5). Strong swirl or organized reservoir motion can place a portion of the total enthalpy in $\bar{u}^2/2$, whereas the station 1 formulation assumes a stagnation reservoir with $\bar{u} = 0$. In that case, the inversion maps a velocity-dependent choking response onto a single thermochemical state. The sign and magnitude of the resulting bias depend on the pressure measurement location, the velocity profile, and the extent to which organized kinetic energy contributes to the effective choked mass flux. Third, species inhomogeneity introduces ambiguity because c^* depends on both thermodynamic state and mixture properties – including MW, γ, heat capacity, and chemical composition. If the composition field near the throat is stratified, the measured choking response reflects an effective composition- and mass-flux-weighted behavior rather than a unique equilibrium or frozen state for the prescribed bulk mixture. In such cases, a single inferred $h_{0,\text{hot}}$ and $T_{0,\text{hot}}$ pair should be interpreted as an effective choking-equivalent state, not as a fully resolved description of the reservoir.

Within this scope, the framework builds upon previous approaches and provides several practical advantages. The inversion is agnostic to test gas and relaxes common single-gas and equilibrium assumptions. It also avoids reliance on energy-balance formulations, temperature-difference measurements, empirical correlations, specialized optical diagnostic setups, or CFD simulations. The method is fully non-intrusive, relies on existing facility instrumentation and open-source thermochemical software, and can be implemented in existing arc-jet facilities without additional diagnostic hardware.

Although the present data was obtained in a single arc-jet facility, the framework is expected to remain facility-agnostic in formulation, provided the following principal assumptions that define the applicability of TSIF remain valid:

1) Fully choked-flow at the nozzle throat.
2) Steady-state conditions during cold-flow and hot-flow measurements.
3) Quasi-one-dimensional upstream reservoir represented by a single effective stagnation state.
4) Negligible upstream kinetic energy relative to total enthalpy ($M \ll 0.3$).
5) Gas-phase thermochemical closure governed by a selectable CEA model (equilibrium or frozen).
6) The discharge coefficient calibrated under cold-flow remains representative during hot-flow operation.

When these assumptions are reasonably satisfied, the present inversion yields a bulk enthalpy quantity that can be meaningfully compared with values inferred using classical sonic-flow, pressure-rise, and calorimetric temperature-rise methods.

III. Experimental methods

Experimental measurements were obtained using the mARC II arc-jet facility to provide the flow observables required by the thermochemical inversion method. The facility configuration, test matrix, and measured quantities used in the analysis are summarized in this section.

A. Arc-jet facility

The mARC II facility is a 30 kW segmented-constricted arc-heater at NASA Ames Research Center. The arc-heater is powered by a Hypertherm MAX200 plasma system, which provides both electrical input and gas-flow control. The device was developed to accelerate the maturation of advanced diagnostics, instrumentation strategies, and material screening methodologies in a laboratory-scale arc-jet environment [5, 35, 46, 49–57]. The overall architecture draws inspiration from larger segmented-constricted facilities at the NASA Ames Arc-Jet Complex [58, 59].

The heater consists of an internal cathode, a modular stack of electrically insulated constrictor disks, an anode, and a convergent–divergent nozzle (see Fig. 4). The second disk has a pressure tap to measure the reservoir pressure upstream of the nozzle. This is the pressure used in the inversion. Since the local Mach number in this region is negligible [60], the measured static pressure is treated as the station 1 total pressure in the quasi-one-dimensional formulation. Once a stable arc column is established, the heated plasma expands through the nozzle into a vacuum test chamber operated at medium vacuum conditions [61]. For all analyzed cold-flow and hot-flow plateaus, the measured the measured downstream-to-upstream pressure ratio p_∞/p_0 remained below the critical pressure ratio for the corresponding gas mixture, so the nozzle was treated as fully choked.

Two heater configurations are employed: "2+0" and "3+1." The first digit denotes the number of constrictor disks between the cathode and the anode, while the second indicates the number of disks located between the anode and the nozzle (often referred to as a mixing plenum segment in the literature). This modular architecture enables variation of effective arc length and plenum volume, thereby altering reservoir pressure, residence time, and mixing characteristics upstream of the nozzle throat.

B. Test matrix and measured quantities

The experimental campaign was designed to evaluate the inversion framework across user-selected gas compositions, mass flow rates, arc-current settings, and heater geometries representative of mARC II operation, with the resulting electrical input power determined by the realized arc voltage–current response. The complete test matrix, including user-selected operating conditions and measured quantities, is summarized in Table 1. For each run, the measured quantities required by the inversion algorithm are:

- Total mass flow rate $\dot{m}_\mathrm{T}$.
- Cold-flow total pressure $p_{0,\mathrm{cold}}$.
- Hot-flow total pressure $p_{0,\mathrm{hot}}$.
- Gas mixture composition Y_i.
- Nozzle throat area A_t (fixed by geometry).

Electrical current and input power are reported for completeness, but are not directly used in the thermochemical inversion. Instead, they provide contextual information regarding heater operating condition and repeatability. Three test gas mixture compositions were investigated to benchmark the inversion framework across chemically distinct environments:

1) CO_2/N_2 ($Y_{CO_2} = 95\%$, $Y_{N_2} = 5\%$) ,
2) Air ($Y_\mathrm{air} = 100\%$) ,
3) N_2 ($Y_{N_2} = 100\%$) .

These mixtures span strongly dissociating air plasmas, single-species nitrogen, and multi-species Mars-relevant mixtures with significant vibrational and dissociation coupling [62]. Conditions A through G span variations in plasma

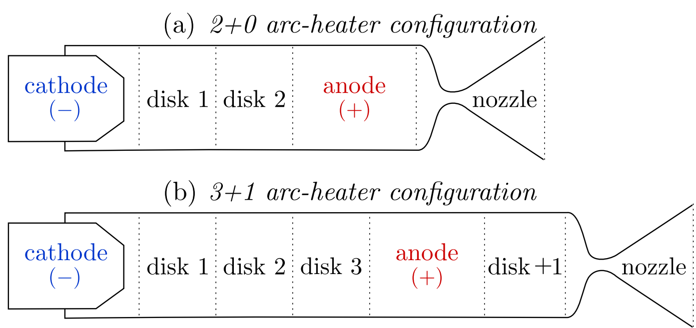

Fig. 4 Segmented-constricted mARC II: 2+0 and 3+1 arc-heater configurations.

Table 1 Experimental test matrix and inferred thermochemical states for mARC II. All enthalpies are referenced to T_{ref} = 298.15 K.

Cond.	Run	Heater	Plasma gas	Shield gas	I_{arc} [A]	P_{arc} [kW]	$\dot{m}_{\mathrm{T}}$ [g/s]	$p_{0,\mathrm{hot}}$ [kPa]	$p_{0,\mathrm{cold}}$ [kPa]	$\frac{p_{0,\mathrm{hot}}}{p_{0,\mathrm{cold}}}$	C_d	$h^{\mathrm{eq}}_{\mathrm{bulk}}$ [MJ/kg]	$h^{\mathrm{fr}}_{\mathrm{bulk}}$ [MJ/kg]	$T^{\mathrm{eq}}_{0,\mathrm{hot}}$ [K]	$T^{\mathrm{fr}}_{0,\mathrm{hot}}$ [K]
A	1	2+0	CO_2 (95%)	N_2 (5%)	200	18.9	0.30	33.1	5.3	6.3	0.84	19.4	21.5	5616	6026
A	2	2+0	CO_2 (95%)	N_2 (5%)	200	18.8	0.30	33.0	5.2	6.3	0.85	19.6	22.0	5667	6091
A	3	2+0	CO_2 (95%)	N_2 (5%)	200	19.8	0.30	32.7	5.4	6.1	0.83	18.9	20.3	5454	5816
A	4	2+0	CO_2 (95%)	N_2 (5%)	200	18.8	0.30	33.3	5.4	6.2	0.83	19.2	21.1	5570	5967
A	5	2+0	CO_2 (95%)	N_2 (5%)	200	18.3	0.30	31.6	5.2	6.0	0.85	18.6	19.7	5359	5692
A	6	2+0	CO_2 (95%)	N_2 (5%)	200	18.6	0.30	31.8	5.2	6.1	0.85	18.8	20.2	5443	5803
A	7	2+0	CO_2 (95%)	N_2 (5%)	200	18.8	0.30	32.5	5.3	6.1	0.84	18.9	20.4	5465	5831
B	8	2+0	Air (100%)	–	40	5.0	0.25	21.9	6.0	3.7	0.73	5.0	5.9	3185	3401
C	9	2+0	Air (100%)	–	150	10.8	0.25	27.2	6.0	4.5	0.73	9.3	10.0	4585	4848
C	10	2+0	Air (100%)	–	200	15.4	0.25	27.5	5.7	4.8	0.76	10.3	11.8	4925	5281
D	11	3+1	Air (100%)	–	150	19.2	0.50	57.4	13.5	4.2	0.65	7.8	8.5	4063	4331
E	12	3+1	Air (100%)	–	150	23.1	0.80	81.1	21.2	3.8	0.66	5.6	6.5	3488	3714
F	13	2+0	N_2 (100%)	–	100	8.9	0.285	21.5	5.6	3.9	0.91	4.8	4.9	4080	4144
G	14	3+1	N_2 (100%)	–	50	7.4	0.40	29.2	8.9	3.3	0.80	3.3	3.3	3025	3026
G	15	3+1	N_2 (100%)	–	150	16.2	0.40	38.1	8.8	4.3	0.81	6.4	7.3	4838	5088

composition, heater configuration (2+0 vs. 3+1), mass flow rate, and pressure ratio. This diversity enables evaluation of the monotonicity, robustness, and chemistry sensitivity of the c^*_{ROCKET}–h_0 inversion across a broad parametric space. Condition A includes repeated runs at nominally identical operating settings in order to quantify measurement repeatability and assess the stability of the inferred bulk enthalpy and total temperature.

IV. Results

This section presents the thermochemical states inferred from the characteristic-velocity inversion and examines how they vary with arc power, specific electrical energy input, gas composition, heater configuration, and chemical model. Internal consistency is then assessed through the self-calibrated discharge coefficient and the hot-flow (arc-on)/cold-flow(arc-off) pressure ratio, followed by comparison of the inferred enthalpies with the classical equilibrium–air sonic-flow correlations of Winovich [11]. Throughout this section, c^*_{ROCKET} denotes the CEA-predicted characteristic velocity defining the c^*_{ROCKET}–h_0 manifold at fixed $p_{0,\mathrm{hot}}$, whereas c^*_{eff} denotes the discharge-corrected experimental query value. The inferred hot-flow state is the unique manifold point $(h_{0,\mathrm{hot}}, T_{0,\mathrm{hot}})$ that matches c^*_{eff}.

Figure 5 shows representative time histories for steady-state plateaus used in the inference $(\dot{m}_{\mathrm{T}}, p_{0,\mathrm{cold}}, p_{0,\mathrm{hot}})$. Cold-flow measurements may be acquired either prior to or following hot-flow operation, depending on facility-specific constraints. In the mARC II arc-jet, such measurements can be performed both before and after arc-on conditions due to the flexibility of the Hypertherm MAX200 power supply, which allows test gas to continue flowing after arc-off. In contrast, at larger arc-jet facilities at NASA Ames Research Center, post-test cold-flow measurements may require substantial power-supply or operating-procedure modifications; as a result, cold-flow operation would likely be limited to pre-arc conditions.

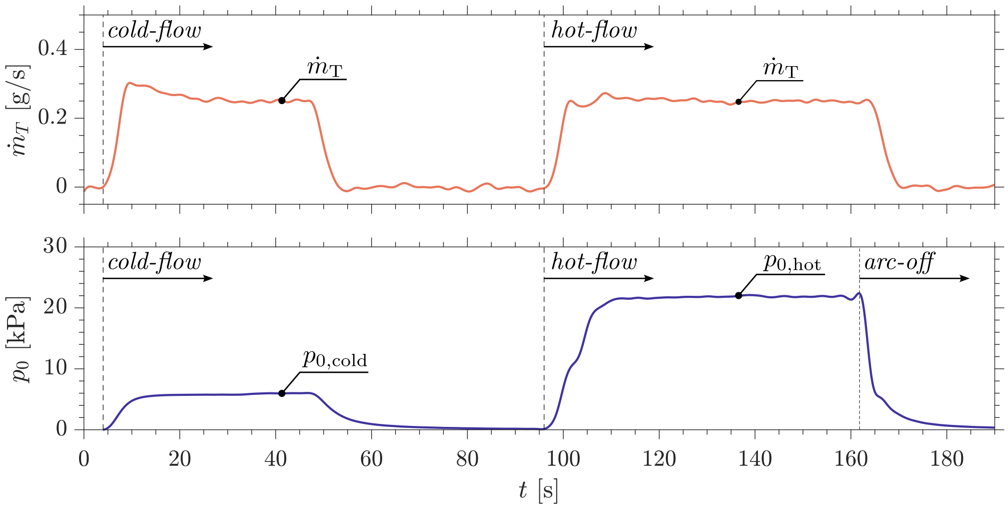

Fig. 5 Representative measured inputs to the inversion algorithm (Run 8): total mass flow rate $\dot{m}_\mathrm{T}$ and upstream total pressure p_0 during cold-flow (arc-off) and hot-flow (arc-on) states.

A. Inferred thermochemical states (h_bulk, $T_{0,\mathrm{hot}}$)

Figure 6 summarizes the thermochemical states inferred from the characteristic-velocity inversion for all test gases and heater configurations. The reported thermochemical state corresponds to the arc-on pair $(h_{0,\mathrm{hot}}, T_{0,\mathrm{hot}})$ obtained at the measured $p_{0,\mathrm{hot}}$ under the selected thermochemical relaxation model (equilibrium or frozen). The primary reported diagnostic is the bulk enthalpy rise h_bulk, while the corresponding total temperature $T_{0,\mathrm{hot}}$ provides a thermodynamically consistent temperature scale associated with the inferred reservoir state.

The top row of Fig. 6 presents the inferred states as a function of arc power P_arc, providing an operational view of how the thermochemical state varies with facility input conditions. The bottom row replots the same states as a function of the specific electrical energy input $P_\mathrm{arc}/\dot{m}_\mathrm{T}$, which provides an energetic interpretation of the arc-heater operating point independent of the particular mass flow configuration. Together, these views illustrate how the inferred bulk enthalpy and total temperature respond to variations in electrical power, mass flow rate, gas composition, and thermochemical model.

1. Arc power and specific energy sensitivity

For subsets in which gas composition, heater configuration, and mass flow rate are approximately fixed, both h_bulk and $T_{0,\mathrm{hot}}$ increase with arc power, as shown in Fig. 6(a,b). This behavior follows directly from the energy balance in arc-heated flow, in which the bulk enthalpy scales approximately with the specific electrical energy input:

$$h_\mathrm{bulk} = \eta \left(\frac{P_\mathrm{arc}}{\dot{m}_\mathrm{T}} \right) , \tag{24}$$

where P_arc is the electrical input power, $\dot{m}_\mathrm{T}$ is the total mass flow rate, and η represents the effective electrical-to-gas coupling efficiency including integrated losses. At fixed $\dot{m}_\mathrm{T}$, increasing P_arc increases the specific electrical energy deposited into the flow, leading to higher inferred bulk enthalpy. The corresponding temperature response depends on how the deposited energy partitions between sensible heating and thermochemical modes, which varies strongly with gas composition (see §IV.A.3).

The CO_2/N_2 cases (Condition A) correspond to nominally repeated operating conditions rather than a deliberate power sweep. Consequently, the modest spread in measured P_arc within this set should be interpreted as run-to-run realization variability. Although Run 3 exhibits the highest measured electrical power within this cluster, it also yields a slightly lower pressure ratio and lower c^*_eff than several neighboring runs. Because the inversion is constrained by the measured choking observables, the inferred thermochemical state for this run is correspondingly lower. This behavior reflects repeatability scatter at nominally fixed conditions rather than a physically meaningful inverse dependence on arc power. The repeated CO_2/N_2 condition also provides a direct repeatability check on the inversion. Across seven nominally repeated runs, the equilibrium solution gives $h^\mathrm{eq}_\mathrm{bulk} = 19.06 \pm 0.36$ MJ/kg and $T^\mathrm{eq}_{0,\mathrm{hot}} = 5511 \pm 109$ K,

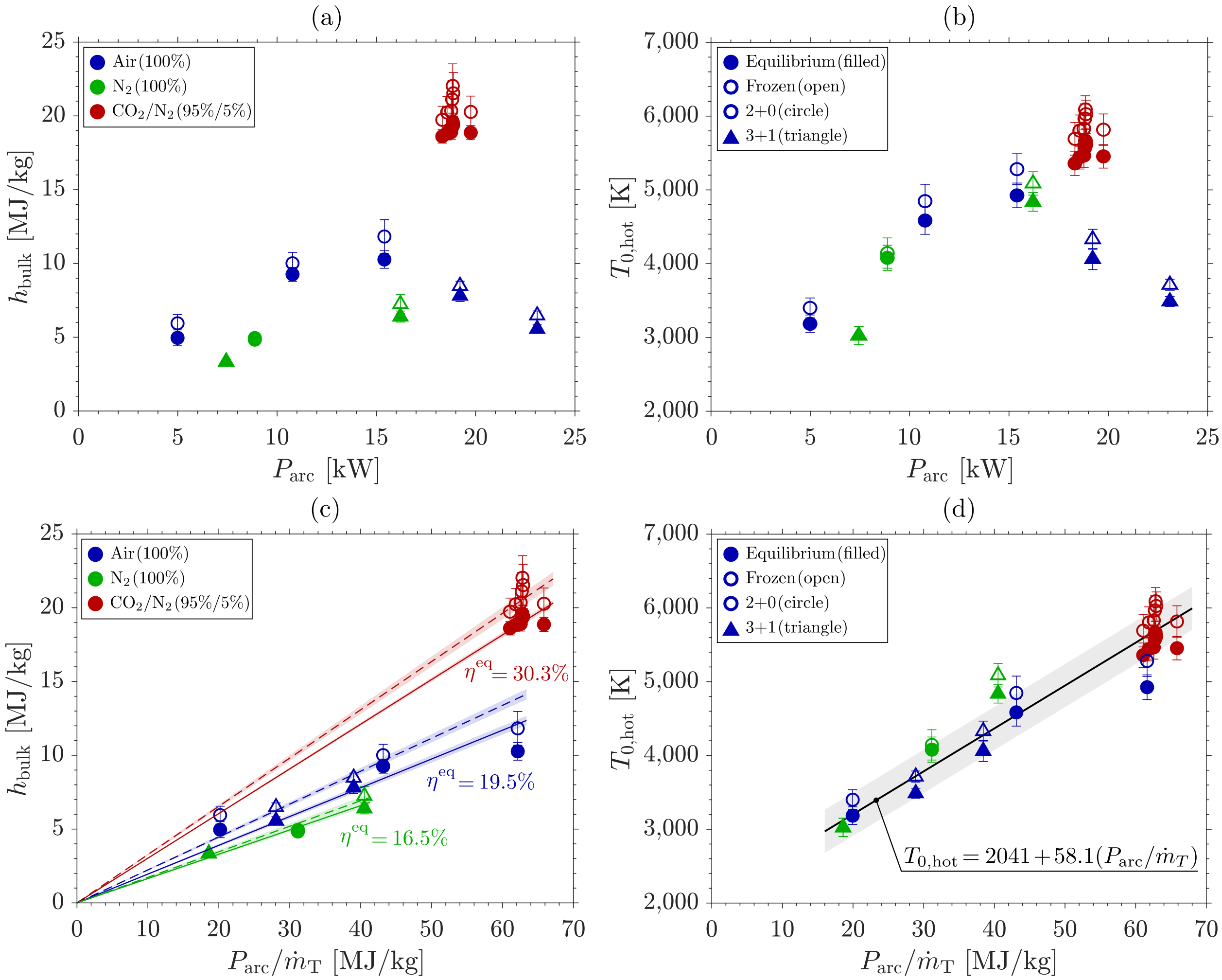

Fig. 6 Inferred thermodynamic states bulk enthalpy h_{bulk} (a,c) and total temperature $T_{0,\text{hot}}$ (b,d): top row as a function of arc power P_{arc} (operational interpretation); bottom row as a function of specific energy input $P_{\text{arc}}/\dot{m}_{\text{T}}$ (energetic interpretation). Error bars indicate $\pm 1\sigma$.

corresponding to run-to-run scatters of approximately 1.9% and 2.0%, respectively. The corresponding frozen solutions give $h^{\text{fr}}_{\text{bulk}} = 20.74 \pm 0.81$ MJ/kg and $T^{\text{fr}}_{0,\text{hot}} = 5889 \pm 142$ K. These repeatability levels indicate that the inversion is stable for nominally repeated CO_2/N_2 operation, with the observed spread attributable primarily to run-to-run operating variability.

The energetic interpretation is illustrated in Fig. 6(c,d), where the same states are plotted against the specific energy input $P_{\text{arc}}/\dot{m}_{\text{T}}$. When expressed in this form, the inferred bulk enthalpy exhibits an approximately linear dependence on specific energy input, consistent with Eq. (24). The corresponding total temperature also increases with specific energy input, as shown in Fig. 6(d). Over the range investigated ($20 \lesssim P_{\text{arc}}/\dot{m}_{\text{T}} \lesssim 70$ MJ/kg), the data exhibit an approximately linear dependence, yielding the empirical fit indicated in the figure. The fitted intercept should not be interpreted as a physical limit, since extrapolation toward lower specific energies would imply temperatures well above realistic inlet conditions. A quadratic fit yields comparable regression quality but produces similarly nonphysical extrapolation. A different functional relationship may apply outside the present range and should be examined when additional data below 20 MJ/kg become available. The linear relation is best interpreted as a local approximation valid within the specific-energy regime explored in the present experiments.

In contrast, the 3+1 cases presented here produce lower h_{bulk} and $T_{0,\text{hot}}$ despite operating at comparable or higher arc powers. This behavior primarily reflects the larger total mass flow rates used for those runs; according to Eq. (24), increasing $\dot{m}_{\text{T}}$ reduces the specific electrical energy input per unit mass and thereby lowers the inferred enthalpy and total temperature. The additional plenum segment in the 3+1 heater increases upstream volume and internal surface area, which may also increase wall heat transfer prior to the nozzle. However, the present dataset does not independently separate this possible configuration effect from the dominant reduction in specific energy input.

Gas-to-gas differences further reflect thermochemical energy partitioning, but the trends in h_{bulk} and $T_{0,\text{hot}}$ are not identical. Among the tested conditions at comparable arc power levels, the inferred bulk enthalpy is highest for CO_2/N_2, followed by air, and then pure N_2. This ordering reflects composition-dependent heat capacity, dissociation, and species redistribution, as described by Eq. (5). Mixtures containing O_2 or CO_2 can store a larger fraction of the deposited electrical energy in chemical and internal modes, leading to greater bulk enthalpy at similar power input. The corresponding total temperature does not follow the same simple gas ordering because it depends on how the deposited energy is partitioned between sensible heating and thermochemical storage.

Taken together, the trends in Fig. 6 show that the inferred thermochemical states respond consistently to variations in electrical input, mass flow rate, heater configuration, and gas composition, supporting the physical consistency of the thermochemically-closed inversion framework.

2. Thermochemical consequences of nitrogen–air substitution

At comparable arc power levels (~16 kW), 100% air and 100% N_2 produce similar inferred total temperatures ($T_{0,\text{hot}} \approx 5{,}000$ K), yet their bulk enthalpies differ substantially (Fig. 6). This behavior reflects the strong composition dependence of thermochemical energy storage in high-temperature reacting gases. As expressed schematically in Eq. (5), the bulk enthalpy of an arc-jet flow mixture includes both sensible thermal energy and chemical energy associated with dissociation and species redistribution. Because air contains O_2, which dissociates more readily than N_2, the effective heat capacity and chemical energy storage differ significantly between air and pure N_2 at comparable total temperature. Equal $T_{0,\text{hot}}$ does not imply equal h_{bulk}, so total temperature alone is insufficient to characterize the energetic state of arc-heated flows. By contrast, h_{bulk} provides an energy-consistent metric across mixtures because it captures both sensible and composition-dependent thermochemical contributions referenced to T_{ref}.

This distinction is particularly relevant because pure nitrogen is often used as a surrogate for air in ground facilities to reproduce high-temperature conditions representative of Earth entry environments [63–69]. For comparable $T_{0,\text{hot}}$, the bulk enthalpy of pure N_2 is substantially lower than that of air because the absence of oxygen eliminates an important thermochemical energy-storage pathway [70]. Since enthalpy strongly influences convective heating and the chemical energy available in the shock layer, substituting N_2 for air can underestimate the energetic state of the flow even when the total temperature appears comparable. These results highlight the importance of working-gas composition in arc-jet test design and reinforce the value of thermochemically resolved flow characterization.

Beyond facility-state interpretation, this composition sensitivity also affects how inferred conditions are used in downstream aerothermal analysis. In high-enthalpy arc-jet environments, stagnation-point heat-transfer correlations for dissociating gases, such as those of Marvin and Deiwert [71], depend directly on the freestream energetic state and associated thermochemical transport properties. Likewise, inverse analyses used to infer catalytic surface properties from measured heat fluxes, such as the framework described by Stewart [6], require a reliable reconstruction of the freestream and shock-layer thermochemical state. In that context, uncertainty in bulk enthalpy propagates into both predicted heating levels and inferred surface reaction parameters. The present inversion framework provides not only a means of estimating the bulk thermochemical state itself, but also a thermodynamically consistent input for subsequent heating and surface-catalysis analyses in arc-jet testing.

3. Effect of chemical model

Across all test conditions shown in Fig. 6, the frozen-chemistry model yields inferred bulk enthalpy h_{bulk} and total temperature $T_{0,\text{hot}}$ values that are equal to or higher than the corresponding equilibrium values. This behavior follows from the thermochemical partitioning of energy described by Eq. (5). Under equilibrium assumptions, species mass fractions adjust continuously with temperature and pressure as the flow accelerates toward the sonic condition, allowing partial recombination as the gas cools. This redistribution of chemical and sensible energy modifies the thermodynamic properties at $M_t = 1$ and therefore the predicted characteristic velocity $c^*_{\text{ROCKET}}(p_0, T_0)$. Matching the same measured c^*_{eff} requires a lower inferred reservoir state under equilibrium chemistry.

In contrast, the frozen model constrains the composition to remain fixed at the stagnation state during acceleration toward the throat. Chemical energy stored in dissociated species cannot relax through recombination, and the thermodynamic properties at the sonic condition reflect the frozen composition. A higher total temperature and bulk enthalpy are then required to satisfy the same measured normalized mass flux $\dot{m}_{\text{T}}/(C_d A_t p_{0,\text{hot}})$.

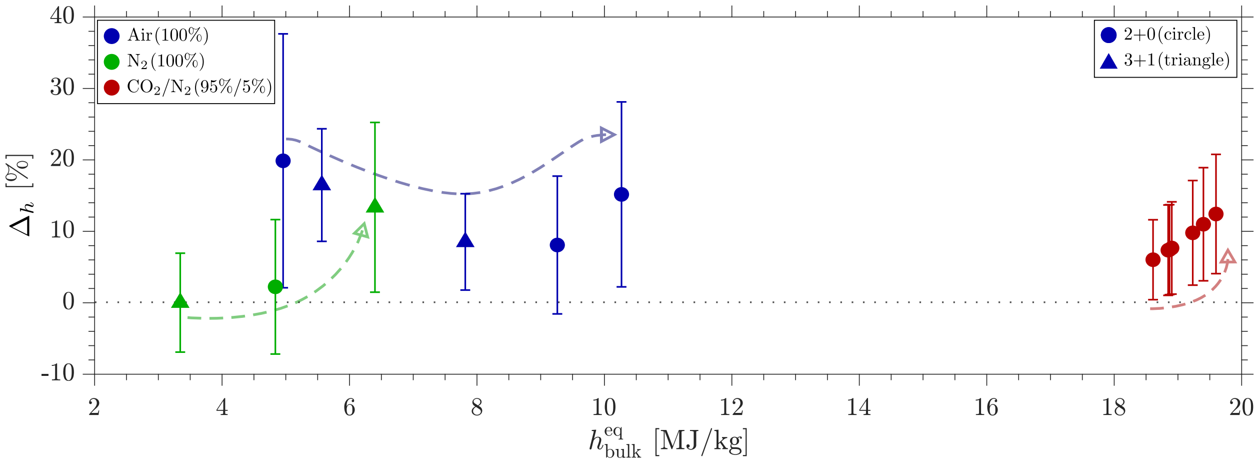

Fig. 7 Relative chemical-model sensitivity of the inferred bulk enthalpy Δ_h from Eq. (25) plotted against equilibrium bulk enthalpy h^{eq}_{bulk} for all gases and heater configurations. Error bars indicate $\pm 1\sigma$ uncertainty.

The difference between the two models depends strongly on the level of thermochemical activity. For the lowest-power nitrogen cases (Conditions F and G at $P_{arc} < 10$ kW), equilibrium and frozen predictions are nearly identical because N_2 dissociation remains weak, leaving the chemical energy contribution in Eq. (5) small.

A contrasting behavior is observed for air at the lowest-power condition (Condition B at $P_{arc} \approx 4.7$ kW), where the frozen and equilibrium predictions differ by $h^{fr}_{bulk} - h^{eq}_{bulk} \approx 1$ MJ/kg and $T^{fr}_{0,hot} - T^{eq}_{0,hot} \approx 225$ K. Unlike pure N_2, air contains O_2, whose dissociation onset occurs at lower temperatures. Oxygen-related chemistry therefore contributes measurable chemical energy storage even in this lower-power regime, producing a finite model sensitivity in both h_{bulk} and $T_{0,hot}$.

The relative difference between frozen and equilibrium enthalpy predictions generally increases with equilibrium bulk enthalpy for fixed-mixture subsets, as shown in Fig. 7. The chemical-model sensitivity is quantified by the relative enthalpy offset:

$$\Delta_h = \left(\frac{h^{fr}_{bulk} - h^{eq}_{bulk}}{h^{eq}_{bulk}} \right) \times 100\% , \tag{25}$$

where the two inferred states correspond to the same measured $\dot{m}_T$, $p_{0,cold}$, $p_{0,hot}$, and gas composition, but different thermochemical relaxation assumptions in the CEA *ROCKET* formulation. Physically, Δ_h measures how strongly the inferred reservoir state must shift when recombination is either permitted (equilibrium) or suppressed (frozen): when equilibrium recombination is significant, quasi-one-dimensional acceleration to the choked condition redistributes internal chemical energy into sensible modes, modifying the sonic-state thermodynamic properties. The same choked-flow constraint can therefore be satisfied at a lower inferred reservoir temperature and enthalpy, leading to $h^{fr}_{bulk} > h^{eq}_{bulk}$ and $\Delta_h > 0$.

For 100% N_2, Δ_h increases monotonically with equilibrium bulk enthalpy because the onset and growth of N_2 dissociation progressively amplify the difference between recombining (equilibrium) and non-recombining (frozen) thermochemical relaxation. At low enthalpy the equilibrium and frozen compositions remain similar, so thermochemical relaxation has little influence on the sonic-state properties and $\Delta_h \approx 0$. As h^{eq}_{bulk} increases, the dissociation fraction rises and recombination becomes increasingly important in the equilibrium solution. The frozen model requires a larger upward shift in the inferred reservoir state to satisfy the same measured choking constraint.

For CO_2/N_2 (95%/5%), Δ_h also increases with h^{eq}_{bulk} but with a different slope because the governing chemistry is dominated by carbon–oxygen partitioning (e.g., $CO_2 \rightleftharpoons CO + O$) rather than the higher-temperature onset of N_2 dissociation. As the mixture enthalpy increases, equilibrium relaxation increasingly redistributes chemical energy through recombination pathways that modify the sonic-state thermodynamic properties. Under frozen chemistry this redistribution is suppressed, leading to a growing separation between the two solutions and an increasing Δ_h. The relatively tight clustering of the CO_2/N_2 points further indicates that, for a fixed mixture, the inferred chemical sensitivity is governed primarily by thermochemistry rather than configuration-dependent departures from ideal choking, which are already represented through the self-calibrated C_d.

The air dataset does not collapse monotonically when plotted against $h_{\mathrm{bulk}}^{\mathrm{eq}}$ alone. A plausible explanation is that the equilibrium–frozen separation depends not only on energy content, but also on the total pressure at which the equilibrium composition is evaluated. Higher $p_{0,\mathrm{hot}}$ promotes molecular recombination, reducing dissociation fractions at a given enthalpy and limiting recombination-driven thermochemical relaxation. As a result, Δ_h may decrease even as $h_{\mathrm{bulk}}^{\mathrm{eq}}$ increases when pressure effects partially offset the growth in dissociation-driven thermochemical activity. The apparent dip at intermediate enthalpy should be interpreted as suggestive of pressure-sensitive equilibrium chemistry rather than as a definitive universal trend. A complete collapse of Δ_h would generally require conditioning on both $h_{\mathrm{bulk}}^{\mathrm{eq}}$ and $p_{0,\mathrm{hot}}$; however, stratifying the air dataset by configuration or pressure bins is limited by the number of available operating points in the present campaign.

Overall, Fig. 7 supports the internal physical consistency of the inversion framework. The chemical-model sensitivity is small when dissociation is weak, increases as thermochemical activity grows within a given mixture, and varies across gases in a manner consistent with their underlying reaction mechanisms. In particular, the distinct behaviors observed for N_2, CO_2/N_2, and air indicate that the framework responds to mixture-dependent thermochemistry, while remaining anchored to the same measured choked-flow constraint.

4. Arc-jet efficiency

The inferred bulk enthalpies can also be used to estimate an arc-jet efficiency for each gas and thermochemical model. From Eq. (24), the slope of h_{bulk} with respect to the specific energy input $P_{\mathrm{arc}}/\dot{m}_{\mathrm{T}}$ provides the effective electrical-to-gas coupling efficiency η. In this context, η should be interpreted as an efficiency inferred from the sonic-flow inversion and the measured electrical input, rather than as an independent calorimetric measurement of individual energy-transfer pathways.

To estimate η, a weighted least-squares regression of Eq. (24) was performed for each gas and thermochemical model, with the fit constrained through the origin, as shown in Fig. 6(c). Each data point was weighted by the inverse variance of the inferred bulk enthalpy. The regression slope provides the mean TSIF-inferred efficiency for the corresponding dataset. Figure 8 shows the efficiencies inferred from individual operating points to illustrate the measurement dispersion about the regression mean.

For the CO_2/N_2 mixture, the inferred efficiencies cluster between approximately 29% and 35% over the investigated range of specific energy input. The measurements scatter about the regression mean without a clear systematic trend with $P_{\mathrm{arc}}/\dot{m}_{\mathrm{T}}$. For air, efficiencies range between roughly 20% and 29%. This dataset exhibits the largest apparent spread, although the limited number of measurements and overlapping uncertainty bounds make it difficult to identify a statistically significant dependence on specific energy input. For pure N_2, the efficiencies fall within a relatively narrow band of approximately 15% to 18%. The measurements form a compact cluster with little variation across the investigated energy range, consistent with an approximately constant efficiency within the experimental uncertainty.

i. Physical interpretation of gas trend

The relative magnitude of the inferred efficiencies follows a physically plausible trend with gas composition. Under equilibrium assumptions, the regression yields $\eta_{\mathrm{CO_2/N_2}}^{\mathrm{eq}} = 30.3\% > \eta_{\mathrm{air}}^{\mathrm{eq}} = 19.5\% > \eta_{\mathrm{N_2}}^{\mathrm{eq}} = 16.5\%$, as shown in Fig. 6(c). These values are TSIF-inferred gas-coupled efficiencies for the present operating envelope.

The observed ordering is consistent with composition-dependent thermochemical energy storage, as suggested by the decomposition in Eq. (5). Within the present reservoir formulation, the upstream kinetic contribution is assumed negligible, so gas-to-gas differences in the recovered h_0 arise primarily through the sensible and chemical-composition terms. From a thermodynamic perspective, the availability of additional internal energy modes increases the effective heat capacity of the gas, allowing deposited energy to be accommodated through vibrational excitation, molecular dissociation, and species redistribution without a proportional increase in temperature. This increase in effective heat capacity is associated with a reduction in the instantaneous effective specific heat ratio $\gamma = c_p/c_v$ and provides a plausible mechanism by which the same electrical input can produce different recovered bulk enthalpies for different gases.

In CO_2-containing mixtures, deposited energy can be accommodated through vibrational excitation, molecular dissociation, and carbon–oxygen species redistribution, affecting both the sensible and chemical-composition contributions in Eq. (5). Air exhibits intermediate behavior because both O_2 and N_2 dissociation contribute to the thermochemical energy budget, whereas pure N_2 is limited primarily to vibrational excitation and dissociation of a single diatomic species over the present temperature range.

At the same time, the present measurements do not independently separate retained gas enthalpy from electrode

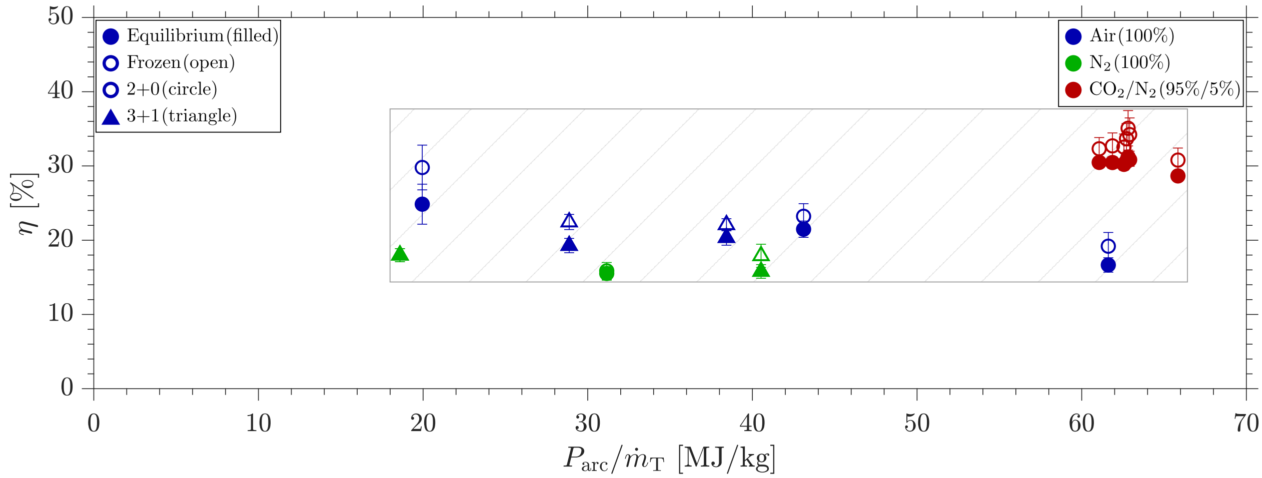

Fig. 8 Arc-jet efficiency η as a function of specific energy input $P_{\mathrm{arc}}/\dot{m}_{\mathrm{T}}$.

heat transfer, wall heat transfer, radiation, arc attachment, or gas-dependent electrical coupling. The efficiency ordering should be interpreted as an effective thermochemical trend inferred from the sonic-flow inversion, not as a direct measurement of the underlying energy partition.

ii. Explanation of constant efficiency

The approximately constant efficiency observed across the investigated range of specific electrical energy input is also physically reasonable. Arc-jet efficiency is governed primarily by discharge characteristics, electrode losses, wall heat transfer, and radiative emission within the plasma column. These mechanisms depend strongly on gas composition and facility geometry, but may vary only weakly with specific energy input over a limited operating regime.

The limited number of operating points in the present dataset further restricts the statistical power required to resolve a weak dependence of η on $P_{\mathrm{arc}}/\dot{m}_{\mathrm{T}}$. Within the explored operating envelope, the efficiency appears approximately constant with specific energy input, which is consistent with the internal behavior of the inversion framework.

B. Discharge coefficient and pressure ratio scaling

Figure 9 provides additional consistency checks on the inversion framework through examination of the self-calibrated discharge coefficient and the hot-flow/cold-flow pressure ratio. For a given gas and heater configuration, the discharge coefficient C_d remains approximately constant across arc power, with variations contained within the $\pm 1\sigma$ bands shown in Fig. 9(a). This relative stability indicates that the cold-flow calibration captures repeatable configuration-dependent departures from ideal quasi-one-dimensional choking, rather than introducing an artificial coupling between C_d and the inferred thermochemical state.

The 2+0 configuration consistently yields higher C_d values than the 3+1 configuration, reflecting differences in the effective choked-flow response of the two heater geometries. As discussed in §II.B, C_d is an effective facility- and nozzle-level correction, not an isolated nozzle coefficient. The lower C_d observed in the 3+1 configuration is consistent with its larger upstream volume, increased wetted surface area, and additional flow-development length prior to the nozzle, which can increase boundary-layer displacement and other departures from ideal choking. The inferred C_d values are lower than discharge coefficients often reported for canonical nozzle flows, where values above ~0.85 and approaching unity are common [36]. This difference is expected because the correction coefficient represents the cumulative choked-flow response of the arc-jet system – including throat geometry, boundary-layer displacement, upstream flow development, radial thermochemical gradients, and configuration-dependent facility effects. The comparatively low values in Fig. 9(a) should therefore be interpreted as a feature of the effective facility-level calibration rather than as an inconsistency of the inversion.

The pressure ratio $p_{0,\mathrm{hot}}/p_{0,\mathrm{cold}}$ shown in Fig. 9(b) increases with arc power for fixed mass flow settings, consistent with the increase in specific electrical energy input. Across gases, the CO_2/N_2 mixture exhibits the highest pressure ratios, followed by air and then pure N_2, mirroring the ordering observed in h_{bulk}. Because the inversion depends on the normalized mass flux $\dot{m}_{\mathrm{T}}/(C_d A_t p_{0,\mathrm{hot}})$, the combined stability of C_d and the physically consistent pressure

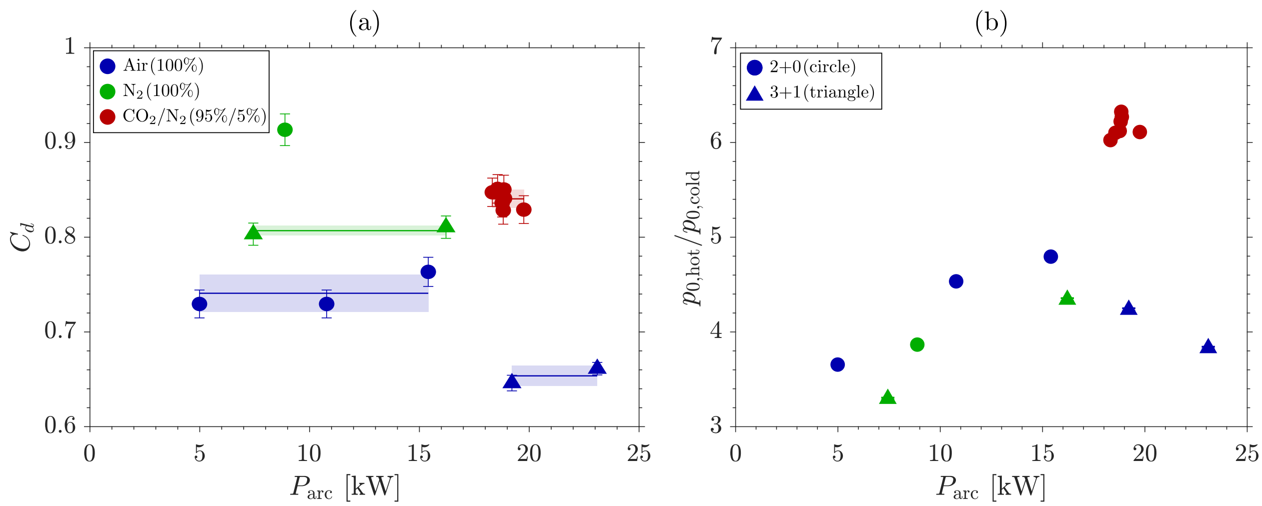

Fig. 9 Inversion consistency metrics as a function of arc power. (a) Self-calibrated discharge coefficient C_d; (b) arc-on to arc-off total pressure ratio $p_{0,\mathrm{hot}}/p_{0,\mathrm{cold}}$. Error bars indicate $\pm 1\sigma$ for each data point in the y-axis. Shaded bands in (a) indicate the mean $\pm 1\sigma$ range for each gas–configuration grouping.

ratio scaling support the interpretation that the inferred thermochemical states are governed by the measured choking response rather than by configuration-dependent departures from ideal choking.

The observed pressure ratio behavior follows directly from the choked-flow relation in Eq. (2) [72]. Applying this relation to the cold-flow and hot-flow states at fixed $\dot{m}_T$ and A_t, with the same effective discharge correction applied to both states, gives:

$$\frac{p_{0,\mathrm{hot}}}{p_{0,\mathrm{cold}}} = \sqrt{\frac{T_{0,\mathrm{hot}}}{T_{0,\mathrm{cold}}}} \frac{\sqrt{\frac{\gamma_{\mathrm{cold}}}{R_{\mathrm{cold}}}} \left(\frac{2}{\gamma_{\mathrm{cold}}+1}\right)^{\frac{\gamma_{\mathrm{cold}}+1}{2(\gamma_{\mathrm{cold}}-1)}}}{\sqrt{\frac{\gamma_{\mathrm{hot}}}{R_{\mathrm{hot}}}} \left(\frac{2}{\gamma_{\mathrm{hot}}+1}\right)^{\frac{\gamma_{\mathrm{hot}}+1}{2(\gamma_{\mathrm{hot}}-1)}}}, \tag{26}$$

where γ and R are evaluated at the corresponding stagnation state.

For N_2 and CO_2/N_2 in the present campaign, $\dot{m}_T$ is effectively constant within each configuration group, so increasing arc power primarily raises $T_{0,\mathrm{hot}}$ and produces the expected monotonic increase in $p_{0,\mathrm{hot}}/p_{0,\mathrm{cold}}$. In contrast, the air dataset spans operating regimes with different $\dot{m}_T$ and $p_{0,\mathrm{cold}}$ values, so the pressure ratio reflects coupled changes in total temperature rise and thermodynamic properties (γ, R) associated with pressure-sensitive equilibrium composition. Equation (26) captures this dependence: higher-energy states require larger $p_{0,\mathrm{hot}}$ relative to $p_{0,\mathrm{cold}}$ to satisfy the same choked mass flow constraint, while gas-dependent property evolution modifies the scaling. The observed ordering across gases and the non-monotonic air behavior are interpreted as consequences of thermochemical-property evolution and changing operating conditions rather than facility artifacts or inconsistencies in the inversion.

This pressure sensitivity also highlights the importance of pressure measurement location. Because the inversion depends explicitly on the measured upstream total pressure, the axial location of the pressure tap can influence the inferred thermochemical state, particularly in larger arc-jet facilities where pressure gradients may arise from frictional (Fanno) or heat-addition (Rayleigh) effects [73]. Although such gradients are modest in the present facility, careful pressure measurement remains essential for accurate enthalpy inference.

Since the inversion is fundamentally constrained by the choked-flow relation linking mass flux and thermochemical state, the resulting h_{bulk} values should remain consistent with classical sonic-flow scaling when the working gas approaches equilibrium air. This expectation is examined explicitly in the following section.

C. Recovery of classical sonic-flow scaling in air

Having demonstrated internal consistency across arc power, gas composition, and chemical model, it is instructive to examine whether the present formulation recovers classical high-enthalpy sonic-flow behavior in the limiting case of air. Because the inversion is constructed from compressible-flow scaling and direct thermochemical closure rather than

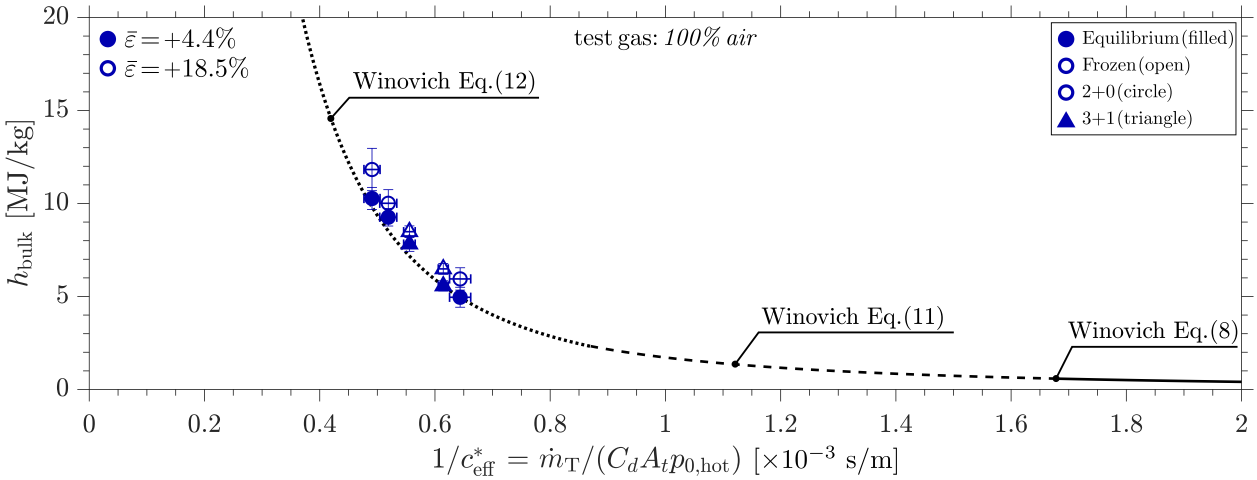

Fig. 10 Comparison of inferred bulk enthalpy for 100% air with the classical equilibrium sonic-flow correlations of Winovich [11].

prescribed air-specific sonic-flow correlations, agreement with established air correlations would indicate that classical sonic-flow behavior emerges naturally from the present framework.

Figure 10 replots the air data as a function of the normalized mass flux $\dot{m}_{\mathrm{T}}/(C_d A_t p_{0,\mathrm{hot}})$, equivalently $1/c^*_{\mathrm{eff}}$. Equations (8), (11), and (12) of Winovich [11], originally formulated in terms of the sonic-flow parameter σ for equilibrium air [5], have been inverted and expressed in SI units to provide an explicit relation between h_{bulk} and normalized mass flux. The Winovich relation used here is the equilibrium-air sonic-flow relation, although the original work also discussed frozen-flow and real-flow corrections. The inferred equilibrium-air enthalpies collapse closely onto the high-enthalpy asymptotic correlation of Winovich [11] (Eq. 12). Quantitatively, the equilibrium dataset exhibits a mean relative residual of +4.4%, a 1σ scatter of 4.4%, and an RMS relative error of 5.9% relative to the Winovich prediction. The small scatter indicates that the present equilibrium-air points follow the classical sonic-flow scaling with high internal consistency, despite differences in facility geometry, pressure and mass flow measurement implementation, discharge calibration, and the use of direct CEA thermochemical inversion rather than the published Winovich equilibrium-air sonic-flow relation. The close agreement obtained without fitting to the Winovich relation provides a strong consistency check on the compressible-flow formulation and thermochemical closure.

The remaining mean offset is plausibly associated with differences between the present CEA-based thermochemical manifold and the thermodynamic data, correction assumptions, facility conditions, and air-heater measurements used to assess the original Winovich formulation. The residuals appear somewhat larger at the higher-enthalpy end of the present air dataset. This trend is plausible because dissociation, recombination sensitivity, and pressure-dependent equilibrium composition become increasingly important as enthalpy rises, making the comparison more sensitive to differences between the present CEA-based manifold and the thermochemical assumptions embedded in the Winovich correlation. Additional equilibrium-air data spanning independently controlled pressure and enthalpy would be required to isolate this dependence.

In contrast, the frozen-chemistry predictions lie systematically above the equilibrium-based Winovich correlation. For the same air dataset, the frozen solutions exhibit a mean relative residual of +18.5% with a 1σ scatter of 1.7%, indicating an approximately uniform upward offset relative to the equilibrium scaling. This systematic separation reflects the thermochemical role of recombination during acceleration to the sonic condition. The Winovich relation plotted here corresponds to equilibrium air, allowing partial recombination as the gas cools toward the throat; this modifies the sonic-state thermodynamic properties and reduces the reservoir enthalpy required to satisfy the choked-flow constraint. In the frozen model, the composition remains fixed at the stagnation state, suppressing recombination-driven energy redistribution and requiring a higher total enthalpy to match the same measured normalized mass flux.

Importantly, when the air data from both heater configurations are expressed in normalized mass flux space, no systematic separation between the 2+0 and 3+1 configurations is observed. The collapse of both configurations onto the same c^*_{ROCKET}–h_0 manifold indicates that, after cold-flow discharge calibration, the inferred equilibrium-air state is governed primarily by the choked-flow constraint rather than by heater-configuration-specific offsets. Configuration effects enter through the measured mass flow, pressure ratio, and calibrated discharge correction, while the underly-

Table 2 Conceptual and methodological comparison between Winovich [11] and the proposed thermochemically-closed sonic-flow inversion framework (TSIF).

	Aspect	*Winovich (1964)*	*Present method (TSIF)*
1.	Primary variable	Sonic-flow parameter for air	Discharge-corrected characteristic velocity c^*_{eff}
2.	Thermochemical treatment	Equilibrium-air baseline with approximate frozen-flow corrections	Selectable CEA equilibrium or frozen model
3.	Gas scope	Air-only sonic-flow formulation	Specified multi-species mixtures supported by thermochemical closure
4.	Enthalpy inference mechanism	Sonic-flow relations between sonic-flow parameter and enthalpy	Direct inversion on a computed $c^*_{\mathrm{ROCKET}} \leftrightarrow h_0$ manifold
5.	Departures from ideal choking	Boundary-layer and discharge-coefficient corrections considered separately	Cold-flow self-calibration of an effective discharge correction
6.	Uncertainty treatment	Tied to sonic-flow relation, correction assumptions, and measurements	Propagated through measured inputs and local manifold sensitivity
7.	Output scope	Bulk enthalpy for air	Bulk enthalpy and paired total temperature for specified multi-species mixtures

ing equilibrium-air thermochemical manifold remains common to both configurations. Agreement of the equilibrium dataset with Winovich's asymptotic relation is not enforced *a priori*, but instead emerges when the working gas is air and equilibrium chemistry is selected. Because the inversion framework is constructed independently of the Winovich air-specific correlation, recovery of Eq. (12) [11] serves as a non-trivial consistency check on the compressible-flow formulation and thermochemical closure rather than a fitting objective.

The conceptual distinctions between the Winovich [11] method and the present inversion framework are summarized in Table 2. While the Winovich formulation provides an air-focused sonic-flow framework with equilibrium-air correlations and approximate correction procedures, the present formulation performs a direct thermochemical inversion for specified gas mixtures and selectable equilibrium or frozen chemical models. In this sense, classical air scaling emerges as a limiting case within a broader thermochemically consistent framework rather than as a governing assumption.

V. Conclusions

A thermochemically-closed sonic-flow inversion framework (TSIF) has been formulated to infer bulk enthalpy and total temperature in arc-heated flows using experimentally accessible upstream quantities. By relying on measured mass flow rate, upstream total pressure, gas composition, nozzle geometry, and cold-flow calibration, the method enables enthalpy and temperature inference without downstream heat-flux, calorimetric, spectroscopic, or CFD-derived inputs. By recasting enthalpy inference in characteristic-velocity space and coupling the inversion directly to a thermochemical solver, the present framework extends the classical air-focused sonic-flow methodology of Winovich [11] to specified multi-species mixtures with selectable thermochemical closure.

The framework was applied to experimental data acquired in the 30 kW mARC II arc-jet facility. Across the test matrix, the inferred thermochemical states follow expected physical trends: h_{bulk} and $T_{0,\mathrm{hot}}$ increase with arc power and specific energy input and decrease when higher mass flow reduces the corresponding specific energy input. Within the present operating envelope, the inferred bulk enthalpy also varies systematically with gas composition, with CO_2/N_2 yielding the highest values, followed by air, and then N_2, reflecting differences in dissociation and thermochemical energy storage. For the tested cases, the 3+1 configuration yields lower inferred values than the 2+0 configuration primarily because of the higher mass flow and corresponding reduction in specific energy input. These trends demonstrate physically consistent scaling within the tested operating envelope and indicate that the inferred states are governed by the measured choking response rather than by uncontrolled scatter in the inversion. In the equilibrium-air limit, the inferred states collapse onto the high-enthalpy asymptotic correlation of Winovich [11] with a mean residual of approximately 4%, confirming that classical sonic-flow scaling is recovered naturally from the formulation rather than imposed through empirical fitting.

The inferred bulk enthalpies also enable characterization of the arc-jet efficiency, enabling gas-dependent electrical-to-flow energy coupling to be estimated from the same framework. In addition, comparison of equilibrium and frozen solutions quantifies the sensitivity of the inferred state to chemical-relaxation assumptions, with frozen chemistry yielding systematically higher inferred enthalpies and total temperatures when recombination effects become important. More broadly, the results show that bulk enthalpy and total temperature are thermochemical state quantities whose accurate inference requires explicit treatment of gas composition and thermochemical closure.

Classical equilibrium-air sonic-flow correlations emerge as limiting cases within a broader inversion framework that is not restricted to published air-specific relations or a single thermochemical relaxation model. In this sense, the present formulation may be viewed as a thermochemically generalized extension of the sonic-flow methodology introduced by Winovich [11], in which air-specific correlations are recast as direct characteristic-velocity inversion with explicit thermochemical closure. By separating measurement physics from thermochemical modeling and propagating uncertainty transparently through the inversion manifold, the method provides a traceable and mixture-flexible framework that is facility-agnostic in formulation, provided the nozzle remains choked and an appropriate cold-flow calibration can be obtained.

Acknowledgments

The author gratefully acknowledges the mARC II team (Dr. Megan E. MacDonald, Joe Hartman, Dr. Magnus Haw, Sebastián V. Colom, Ramon Martinez, Ryan Chung, Daniel Philippidis, Enrique Carballo, Kate Edwards, Jacob Weiland, Alejandro Contreras, Jacob Torres, Daniel Lehr, James Hope, Nicholas Reed, Amelia Kinsella, Frank Hui, Aidan Ross), TS leadership (Peter Race, Scott Eddleman, Dr. David Hash) and John Balboni for their technical mentorship as well as institutional support of the mARC II facility and its modernization efforts.

Funding Sources

Jocelino Rodrigues is the recipient of a NASA Postdoctoral Program (NPP) research fellowship at NASA Ames Research Center, administered by Oak Ridge Associated Universities (ORAU) under the NASA contract 80HQTR21CA005.

Data Availability Statement

The NASA Chemical Equilibrium with Applications (CEA) code used for thermochemical calculations is publicly available at https://github.com/nasa/cea. CEA was selected for the present implementation because it is publicly available and enables reproducible construction of the thermochemical manifolds used in the inversion. The inversion framework developed in this study was implemented using standard CEA calls and custom post-processing routines. Experimental data supporting the findings of this study are available from the corresponding author upon reasonable request.

References

[1] Calomino, A., Bruce, W., Gage, P., Horn, D., Mastaler, M., Rigali, D., Robey, J., Voss, L., Wahlberg, J., and Williams, C., "Evaluation of the NASA Arc Jet Capabilities to Support Mission Requirements [NASA/SP-2010-577]," Office of the Chief Engineer, 2010, URL: http://hdl.handle.net/2060/20110007355.

[2] MacDonald, M., Rodrigues, J., Cushman, G., Martin, K., and Hartman, J., "Simultaneous Convective and Radiative Heating of Materials with the 200 kW Laser Enhanced Arc Jet Facility (LEAF)," *National Space & Missile Materials Symposium and Commercial and Government Responsive Access to Space Technology Exchange (NSMMS & CRASTE) Joint Symposia*, Tucson, AZ, 2023, pp. 1–18. URL: https://ntrs.nasa.gov/citations/20230008351.

[3] Gasch, M., Hwang, H., Ellerby, D., Stackpoole, M., Venkatapathy, E., Cassell, A., Feldman, J., Muppidi, S., Beck, R., White, T., and Chaffey, M., "Technologies for Future Venus Exploration," *Bulletin of the AAS*, Vol. 53, No. 4, 2021. DOI: 10.3847/25c2cfeb.a50740a5.

[4] MacDonald, M. E., Balboni, J., Cornelison, C., Hartman, J., Haw, M., Fretter, E., Cruden, B., Wilder, M., and Hwang, H., "NASA Ames Thermophysics Ground Test Facilities Supporting Future Planetary Atmospheric Entry," *Bulletin of the AAS*, Vol. 53, No. 4, 2021. DOI: 10.3847/25c2cfeb.49be7320.

[5] Palmer, G. E., Prabhu, D. K., Rodrigues, J., Driver, D. M., and Balboni, J. A., "CFD Simulations of Arcjet Experiments – A Survey of Recommended Practices and Lessons Learned," *AIAA AVIATION FORUM AND ASCEND 2025*, American Institute of Aeronautics and Astronautics, Reston, Virginia, 2025. DOI: 10.2514/6.2025-3480.

[6] Stewart, D. A., "Surface Catalysis and Characterization of Proposed Candidate TPS for Access-to-Space Vehicles [TM 112206]," NASA Ames Research Center, Moffett Field, CA, 1997, URL: https://ntrs.nasa.gov/citations/19970026958.

[7] Peters, A. B., Zhang, D., Chen, S., Ott, C., Oses, C., Curtarolo, S., McCue, I., Pollock, T. M., and Prameela, S. E., "Materials design for hypersonics," *Nature Communications*, Vol. 15, No. 1, 2024, p. 3328. DOI: 10.1038/s41467-024-46753-3.

[8] Park, C., *Nonequilibrium Hypersonic Aerothermodynamics*, Wiley, 1990.

[9] Zuppardi, G., and Mongelluzzo, G., "Aerothermochemical analysis of the Orion capsule in rarefied transitional flow regime during Mars entry," *Advances in Space Research*, Vol. 69, No. 7, 2022, pp. 2825–2835. DOI: 10.1016/j.asr.2022.01.013.

[10] Smith, D. M., and Felderman, E., "Aerothermal Testing of Space and Missile Materials in the Arnold Engineering Development Center Arc Jet Facilities," *25th AIAA Aerodynamic Measurement Technology and Ground Testing Conference*, American Institute of Aeronautics and Astronautics, Reston, Virginia, 2006, pp. 528–549. DOI: 10.2514/6.2006-3293.

[11] Winovich, W., "On the equilibrium sonic-flow method for evaluating electric-arc air-heater performance (NASA TN D-2132)," NASA Ames Research Center, 1964, URL: https://archive.org/details/nasa_techdoc_19640007240.

[12] Shepard, C., Milos, F., and Taunk, J., "A sonic flow equation for electric arc jets," *24th Plasma Dynamics, and Lasers Conference*, American Institute of Aeronautics and Astronautics, Reston, Virginia, 1993, pp. 1–9. DOI: 10.2514/6.1993-3183.

[13] Sharma, S., Park, C., Scott, C., Arepalli, S., and Taunk, J., "Arcjet flow characterization," *34th Aerospace Sciences Meeting and Exhibit*, American Institute of Aeronautics and Astronautics, Reston, Virigina, 1996. DOI: 10.2514/6.1996-612.

[14] Park, C., Raiche, G. A., Driver, D. M., Olejniczak, J., Terrazas-Salinas, I., Hightower, T. M., and Sakai, T., "Comparison of enthalpy determination methods for arc-jet facility," *Journal of Thermophysics and Heat Transfer*, Vol. 20, No. 4, 2006, pp. 672–679. DOI: 10.2514/1.15744.

[15] Thompson, C., Prabhu, D., Terrazas-Salinas, I., and Mach, J., "Bulk Enthalpy Calculations in the Arc Jet Facility at NASA ARC," *42nd AIAA Thermophysics Conference*, American Institute of Aeronautics and Astronautics, Reston, Virginia, 2011, pp. 1–10. DOI: 10.2514/6.2011-3475.

[16] Prabhu, D., Saunders, D., Oishi, T., Skokova, K., Santos, J., Fu, J., Terrazas-Salinas, I., Carballo, J., and Driver, D., "CFD Analysis Framework for Arc-Heated Flowfields I: Stagnation Testing in Arc-Jets at NASA ARC," *41st AIAA Thermophysics Conference*, American Institute of Aeronautics and Astronautics, Reston, Virginia, 2009. DOI: 10.2514/6.2009-4080.

[17] Prabhu, D., Saunders, D., Oishi, T., Skokova, K., Santos, J., Fu, J., Terrazas-Salinas, I., Carballo, E., and Driver, D., "CFD analysis framework for arc-heated flowfields, II: Shear Testing in Arc-jets at NASA ARC," *41st AIAA Thermophysics Conference*, 2009. DOI: 10.2514/6.2009-4081.

[18] ASTM International, "Standard Practice for Measuring Plasma Arc Gas Enthalpy by Energy Balance [ASTM E341–08]," ASTM International, 2020, DOI: 10.1520/E0341-08R20.

[19] Scott, C., Suess, L., Milhoan, J., Oelke, L., Godfrey, D., Larin, M., Grinstead, J., and Del Papa, S., "Enthalpy Distributions of Arc Jet Flow Based on Measured Laser Induced Fluorescence, and Heat Flux and Stagnation Pressure Distributions," *42nd AIAA Thermophysics Conference*, American Institute of Aeronautics and Astronautics, Reston, Virigina, 2011. DOI: 10.2514/6.2011-3778.

[20] Boulos, M. I., "The inductively coupled R.F. (radio frequency) plasma," *Pure and Applied Chemistry*, Vol. 57, No. 9, 1985, pp. 1321–1352. DOI: 10.1351/pac198557091321.

[21] Grinstead, J., Porter, B., and Carballo, E., "Flow Property Measurements Using Laser-Induced Fluorescence in the NASA Ames Interaction Heating Facility Arc Jet," *49th AIAA Aerospace Sciences Meeting including the New Horizons Forum and Aerospace Exposition*, American Institute of Aeronautics and Astronautics, Reston, Virigina, 2011. DOI: 10.2514/6.2011-1091.

[22] Finch, P. M., Granowitz, Z. N., Strand, C. L., MacDonald, M. E., and Hanson, R. K., "Measurements of Temperature and Enthalpy in NASA Ames 60-MW Arcjet using Atomic Oxygen and Atomic Nitrogen Absorption," *AIAA SCITECH 2023 Forum*, American Institute of Aeronautics and Astronautics, Reston, Virginia, 2023. DOI: 10.2514/6.2023-2333.

[23] Sander, T., Lettl, M., Walter, C., and Mundt, C., “Two-dimensional laser-induced fluorescence thermometry in a medium- to high-enthalpy CO2 flow,” *Applied Physics B*, Vol. 129, No. 4, 2023, p. 63. DOI: 10.1007/s00340-023-07997-x.

[24] Finch, P. M., Granowitz, Z. N., Strand, C. L., Hanson, R. K., MacDonald, M. E., Hui, F. C. L., and Gökçen, T., “Temperature and Enthalpy Characterization of NASA Arcjet Using Oxygen and Nitrogen Absorption,” *Journal of Thermophysics and Heat Transfer*, Vol. 39, No. 4, 2025, pp. 936–955. DOI: 10.2514/1.T7088.

[25] Meyers, J. M., Kumar, S., Munafò, A., and Panesi, M., “Simultaneous O Atom nsTALIF and NO nsLIF Imaging Strategy to Expedite Characterization and Numerical Validation of High Enthalpy Plasma Flows,” *AIAA SCITECH 2026 Forum*, American Institute of Aeronautics and Astronautics, Reston, Virginia, 2026. DOI: 10.2514/6.2026-2462.

[26] Meyers, J. M., Singh, A., Munafò, A., and Panesi, M., “Gas Surface Interaction Reactant and Product Characterization in High Enthalpy Air Plasma Flows via nsTALIF/LIF Imaging in the UIUC 350 kW Plasmatron X Facility,” *AIAA SCITECH 2026 Forum*, American Institute of Aeronautics and Astronautics, Reston, Virginia, 2026. DOI: 10.2514/6.2026-2463.

[27] Gupta, R. N., Yos, J. M., Thompson, R. A., and Lee, K.-P., “A Review of Reaction Rates and Thermodynamic and Transport Properties for an 11-Species Air Model for Chemical and Thermal Nonequilibrium Calculations to 30,000 K [RP 1232],” NASA, 1990, URL: https://ntrs.nasa.gov/citations/19900017748.

[28] Park, C., “Review of chemical-kinetic problems of future NASA missions. I - Earth entries,” *Journal of Thermophysics and Heat Transfer*, Vol. 7, No. 3, 1993, pp. 385–398. DOI: 10.2514/3.431.

[29] Aiken, T. T., and Boyd, I. D., “Two-Temperature Modeling of Nonequilibrium Relaxation and Dissociation in Shock-Heated Oxygen,” *Journal of Thermophysics and Heat Transfer*, Vol. 37, No. 4, 2023, pp. 723–732. DOI: 10.2514/1.t6753.

[30] Capriati, M., Turchi, A., Congedo, P. M., and Magin, T. E., “Holistic characterization of an under-expanded high-enthalpy jet under uncertainty,” *Physics of Fluids*, Vol. 36, No. 6, 2024. DOI: 10.1063/5.0203490.

[31] Donohue, J., Fletcher, D., and Park, C., “Emission spectral measurements in the plenum of an arc-jet wind tunnel,” *7th AIAA/ASME Joint Thermophysics and Heat Transfer Conference*, American Institute of Aeronautics and Astronautics, Reston, Virigina, 1998, p. 2946. DOI: 10.2514/6.1998-2946.

[32] Cipullo, A., Savino, L., Marenna, E., and De Filippis, F., “Thermodynamic state investigation of the hypersonic air plasma flow produced by the arc-jet facility SCIROCCO,” *Aerospace Science and Technology*, Vol. 23, No. 1, 2012, pp. 358–362. DOI: 10.1016/j.ast.2011.09.002.

[33] Hermann, T., Löhle, S., Fasoulas, S., and Andrianatos, A., “Tomographic optical emission spectroscopy of a high enthalpy air plasma flow,” *Applied Optics*, Vol. 55, No. 36, 2016, p. 10290. DOI: 10.1364/AO.55.010290.

[34] Hermann, T., Löhle, S., Zander, F., and Fasoulas, S., “Measurement of the aerothermodynamic state in a high enthalpy plasma wind-tunnel flow,” *Journal of Quantitative Spectroscopy and Radiative Transfer*, Vol. 201, 2017, pp. 216–225. DOI: 10.1016/j.jqsrt.2017.06.022.

[35] Colom, S. V., Haw, M. A., and Rodrigues, J., “Design and implementation of a fast-sweeping Langmuir probe diagnostic for DC arc jet environments,” *Review of Scientific Instruments*, Vol. 96, No. 11, 2025. DOI: 10.1063/5.0272186.

[36] Sutton, G., and Biblarz, O., *Rocket Propulsion Elements*, 7th ed., Wiley, 2001.

[37] McBride, B. J., and Gordon, S., “Computer Program for Calculating and Fitting Thermodynamic Functions,” NASA, 1992, URL: https://ntrs.nasa.gov/citations/19930003779.

[38] McBride, B. J., and Gordon, S., “Computer Program for Calculation Complex Chemical Equilibrium Compositions and Applications: II. Users Manual and Program Description,” NASA, 1996, URL: https://ntrs.nasa.gov/citations/19960044559.

[39] Gordon, S., and McBride, B. J., “Computer Program for Calculation Complex Chemical Equilibrium Compositions and Applications: I. Analysis,” NASA, 1994, URL: https://ntrs.nasa.gov/citations/19950013764.

[40] Gordon, S., and McBride, B., “Thermodynamic Data to 20 000 K for Monatomic Gases [TP 208523],” NASA, 1999, URL: https://ntrs.nasa.gov/citations/19990063361.

[41] McBride, B. J., Gordon, S., and Reno, M. A., “Thermodynamic Data for Fifty Reference Elements [TP 3287/REV1],” NASA, 2001, URL: https://ntrs.nasa.gov/citations/20010021116.

[42] Zehe, M. J., Gordon, S., and Mcbride, B. J., “CAP: A Computer Code for Generating Tabular Thermodynamic Functions from NASA Lewis Coefficients [TP 210959/REV1],” NASA, 2002, URL: https://ntrs.nasa.gov/citations/20020012428.

[43] Leader, M., "NASA CEA (Chemical Equilibrium with Applications): GitHub repository," 2026. URL: https://github.com/nasa/cea.

[44] Anderson Jr., J. D., *Hypersonic and High-Temperature Gas Dynamics, Second Edition*, American Institute of Aeronautics and Astronautics, Reston ,VA, 2006. DOI: 10.2514/4.861956.

[45] Shepard, C. E., Ketner, D. M., and Vorreiter, J. W., "A High-Enthalpy Plasma Generator for Entry Heating Simulation [TN-D-4583]," NASA, 1968, URL: https://ntrs.nasa.gov/citations/19680015088.

[46] Palmer, G. E., Prabhu, D., Driver, D. M., Rodrigues, J., and Balboni, J. A., "Computational Fluid Dynamics Simulations of Arcjet Experiments: Recommended Practices and Lessons Learned," *Journal of Thermophysics and Heat Transfer*, 2026, pp. 1–25. DOI: 10.2514/1.T7311.

[47] Rodrigues, J., Rolland, E. O., De Domenico, F., and Hochgreb, S., "Computational investigation of direct noise generated by synthetic hot spots in a duct," *24th International Congress on Sound and Vibration*, London, 2017, pp. 1–8. DOI: 10.1016/j.jsv.2017.01.004.

[48] De Domenico, F., Rolland, E. O., Rodrigues, J., Magri, L., and Hochgreb, S., "Compositional and entropy indirect noise generated in subsonic non-isentropic nozzles," *Journal of Fluid Mechanics*, Vol. 910, 2021, p. A5. DOI: 10.1017/jfm.2020.916.

[49] Codron, D. A., and Nawaz, A., "Radial Profiles of Plasma Electron Characteristics in a 30 kW Arc Jet," *44th AIAA Plasmadynamics and Lasers Conference*, American Institute of Aeronautics and Astronautics, Reston, Virginia, 2013, pp. 1–12. DOI: 10.2514/6.2013-3128.

[50] Codron, D. A., Cruden, B. A., and Ho, T., "Emission Spectroscopy Characterization of Thermal Protection System Materials in Arc-Heated Flows," *45th AIAA Plasmadynamics and Lasers Conference*, American Institute of Aeronautics and Astronautics, Reston, Virginia, 2014, p. 2112. DOI: 10.2514/6.2014-2112.

[51] Miller, R. A., Tang, C. Y., McGlaughlin, M. S., White, T. R., Ho, T. S., MacDonald, M. E., and Cruden, B. A., "Characterization of a radiometer window for Mars aftbody heating including ablation product deposition using a miniature arc jet," *2018 Joint Thermophysics and Heat Transfer Conference*, American Institute of Aeronautics and Astronautics, Reston, Virginia, 2018, pp. 1–17. DOI: 10.2514/6.2018-3590.

[52] Luís, D., and MacDonald, M. E., "Emission spectroscopy characterization of electrode species in the freestream flow at the NASA Ames miniature Arc Jet II facility," *Journal of Quantitative Spectroscopy and Radiative Transfer*, Vol. 272, 2021, p. 107752. DOI: 10.1016/j.jqsrt.2021.107752.

[53] Haw, M. A., MacDonald, M. E., and Colom, S. V., "Big-data Efficient and Automated Science Transfer (BEAST): an open-source software architecture for arc jet data management, modeling, and automation," *AIAA SCITECH 2023 Forum*, American Institute of Aeronautics and Astronautics, Reston, Virginia, 2023, pp. 1–16. DOI: 10.2514/6.2023-2712.

[54] Marshall, P., Caldwell, A., Feldman, J., Chavez-Garcia, J., Hendrickson, K., Rodrigues, J., MacDonald, M., Turcotte, A., Alcantara, T., Swaiss, C., and Bebak, A., "Designing Insulative Reusable Thermal Protection Materials – from Shuttle Tile to Next Generation Systems," *Composites, Materials, & Structures (CMS 2025) 48th Annual Conference*, 2025.

[55] V. Colom, S., A. Haw, M., and Rodrigues, J., "First Characterization of RF Plasma Jet Using Spatially-Resolved OES and Fast-Sweeping Langmuir Diagnostics," *67th Annual Meeting of the APS Division of Plasma Physics (DPP)*, Long Beach, California, 2025. URL: https://archive.aps.org/dpp/2025/po06/4/.

[56] Rodrigues, J., "Closed-Form Reconstruction of Zoby–Sullivan Stagnation-Point Heat-Flux Scaling," *Journal of Thermophysics and Heat Transfer*, 2026.

[57] Edwards, K. M., Rodrigues, J., and Philippidis, D., "Extending mARC II Arc-Jet Test Duration via Design and Implementation of Model System Cooling Sleeve," *AIAA AVIATION 2026 FORUM*, 2026.

[58] Terrazas-Salinas, I., "Test Planning Guide for NASA Ames Research Center Arc Jet Complex and Range Complex [A029-9701-XM3 Rev. J – July 28, 2022]," NASA Ames Research Center, 2022, URL: https://www.nasa.gov/wp-content/uploads/2023/07/tsf-test-planning-guide-revj.pdf.

[59] MacDonald, M. E., Haw, M. A., Martinez, R., Colom, S., Rodrigues, J., Chung, R., and Hartman, J., "Characterizing Heat Flux in the miniature Arc jet Research Chamber (mARC II)," *AIAA AVIATION 2023 Forum*, American Institute of Aeronautics and Astronautics, San Diego, California, 2023, pp. 1–9. DOI: 10.2514/6.2023-3298.

[60] Rodrigues, J., Macdonald, M. E., Haw, M. A., Martinez, R., Philippidis, D., Colom, S., Chung, R., and Hartman, J., "Defining the Operational Envelope for Air Flows in the miniature Arc jet Research Chamber (mARC II)," *AIAA AVIATION FORUM AND ASCEND 2024*, AIAA, Las Vegas, Nevada, 2024. DOI: 10.2514/6.2024-3553.

[61] Rodrigues, J., MacDonald, M. E., Haw, M., Martinez, R., Philippidis, D., Colom, S., Chung, R. J., and Hartman, J., "Expanding the Measurement Capabilities of the mARC II Arc-Jet to Map the Operating Envelope for High-Enthalpy Air Flows," *AIAA SCITECH 2025 Forum*, American Institute of Aeronautics and Astronautics, Reston, Virginia, 2025. DOI: 10.2514/6.2025-2443.

[62] Splinter, S., Bey, K., Gragg, J., and Brewer, A., "Comparative Measurements of Earth and Martian Entry Environments in the NASA Langley HYMETS Facility," *49th AIAA Aerospace Sciences Meeting including the New Horizons Forum and Aerospace Exposition*, American Institute of Aeronautics and Astronautics, Reston, Virigina, 2011, p. 1014. DOI: 10.2514/6.2011-1014.

[63] Fletcher, D. G., "Arcjet flow properties determined from laser-induced fluorescence of atomic nitrogen," *Applied Optics*, Vol. 38, No. 9, 1999, p. 1850. DOI: 10.1364/AO.38.001850.

[64] Düzel, U., Schroeder, O. M., Zhang, H., and Martin, A., "Numerical simulation of an arc jet test section," *Journal of Thermophysics and Heat Transfer*, Vol. 34, No. 2, 2020, pp. 393–403. DOI: 10.2514/1.T5722.

[65] Chatzigeorgis, G. B., Schroeder, O. M., Schulz, J. C., Palmer, G., Stern, E. C., and Martin, A., "Coupled Fluid Dynamics and Material Response simulations for Nitrogen Arc Jet flows," 2024. DOI: 10.2514/6.2024-3815.

[66] Franco, M., Capponi, L., Oruganti, S., Elliott, G. S., and Panerai, F., "Investigation of Slug Calorimeter Heat Flux Measurements in the Plasmatron X Wind Tunnel," *AIAA SciTech Forum and Exposition, 2024*, American Institute of Aeronautics and Astronautics Inc, AIAA, 2024. DOI: 10.2514/6.2024-1900.

[67] Chaplygin, A., Yakimov, M., Vasil'evskii, S., Kotov, M., Lukomskii, I., Galkin, S., Shemyakin, A., Solovyov, N., and Kolesnikov, A., "Combined Plasma and Laser Heating of Graphite," *Plasma*, Vol. 8, No. 1, 2025, p. 9. DOI: 10.3390/plasma8010009.

[68] Samuels, K. E., Isaacs, C. T., and Baccarella, D., "Emission Spectroscopy Through Converging–Diverging Nozzle of Hypersonic Arcjet Tunnel," *AIAA Journal*, 2025, pp. 1–15. DOI: 10.2514/1.J065739.

[69] Samuels, K. E., and Baccarella, D., "Nonequilibrium analysis of emission spectra in the plenum chamber of an arcjet wind tunnel," *Aerospace Science and Technology*, Vol. 172, 2026, p. 111721. DOI: 10.1016/j.ast.2026.111721.

[70] Brune, A. J., Bruce, W. E., Glass, D. E., and Splinter, S. C., "Computational Predictions of the Hypersonic Material Environmental Test System Arcjet Facility," *Journal of Thermophysics and Heat Transfer*, Vol. 33, No. 1, 2019, pp. 199–209. DOI: 10.2514/1.T5490.

[71] Marvin, J. G., and Deiwert, G. S., "Convective heat transfer in planetary gases." *AIAA Journal*, Vol. 4, No. 4, 1966, pp. 727–728. DOI: 10.2514/3.3523.

[72] Anderson, J. D., *Modern Compressible Flow: with Historical Perspective*, 2nd ed., McGraw-Hill, 1990.

[73] Shapiro, A. H., *The Dynamics and Thermodynamics of Compressible Fluid Flow*, Ronald Press, New York, 1953.